This is a preprint of: "Ballistic Transfers Across the 1:1 Resonance Around Vesta Following Invariant Manifolds", José María Mondelo, Stephen B. Broschart, Benjamin F. Villac, *J. Guidance Control Dynam.*, vol. 36(4), 1119–1133, 2013.
DOI: [10.2514/1.57494]

# Ballistic Transfers Across the 1:1 Resonance Around Vesta Following Invariant Manifolds[1]

Josep-Maria Mondelo[2]
*Universitat Autònoma de Barcelona,*

*08193 Bellaterra (Barcelona), Spain*

Stephen B. Broschart[3]
*Jet Propulsion Laboratory, California Institute of Technology,*

*4800 Oak Grove Drive, Pasadena, CA 91109, USA*

Benjamin F. Villac[4]
*University of California at Irvine,*

*Irvine, CA 92617, USA*

**Motivated by the challenging crossing of the 1:1 resonance planned for the Dawn mission, a general transfer design strategy is developed using the manifold structure of near-synchronous, unstable periodic orbits. Two families of transfers across the 1:1 resonance at the asteroid Vesta demonstrate the approach. A family of low-inclination, low-energy transfers follows the stable and unstable manifolds of the libration orbits near Vesta's equilibrium points (in a surface-fixed rotating frame). A high inclination family of transfers arises similarly from the manifold structure of near-polar, near-circular orbits. Ballistic, resonance crossing transfers near Vesta are presented and characterized. This transfer design methodology applies well to any solar system body where the dynamics are dominated by gravitational acceleration from a non-spherical central-body potential.**

---


[2] Associate Professor, Departament de Matemàtiques. AIAA member. Email: jmm@mat.uab.cat
[3] Mission Design Engineer; Navigation and Mission Design Section, M/S 301-121. AIAA senior member. Email: Stephen.B.Broschart@jpl.nasa.gov
[4] Assistant Professor, University of California, Irvine; Mechanical and Aerospace Engineering, 4200 Engineering Gateway, Irvine, CA 92697-3975. AIAA member. Email: bvillac@uci.edu

**Nomenclature**

| | | |
|---|---|---|
| $\tilde{\mathbf{r}} = (x, y, z)$ | = | spacecraft position vector in body-fixed, Vesta centered frame |
| $(r, \phi, \lambda)$ | = | radius, latitude and longitude of spacecraft in the Vesta centered, body-fixed frame |
| $\boldsymbol{\omega}, \omega$ | = | angular velocity vector of Vesta (relative to inertial space) and associated magnitude |
| $U,\ \mu$ | = | Vesta gravitational field force potential and parameter |
| $R_V$ | = | radius of the reference sphere associated with the spherical harmonic gravity field |
| $\bar{C}_{nm}, \bar{S}_{nm}$ | = | normalized spherical harmonic coefficients of the gravitational field |
| $P_n$ | = | Legendre polynomials |
| $P_{nm}, \bar{P}_{nm}$ | = | associated Legendre and normalized associated Legendre functions |
| $\tilde{\mathbf{p}} = (p_x, p_y, p_z)$ | = | orbiter momenta in rotating, body-fixed Vesta centered frame |
| $H(\tilde{\mathbf{r}}, \tilde{\mathbf{p}})$ | = | orbiter Hamiltonian, also referred to as energy |
| $h$ | = | arbitrary fixed value of the Hamiltonian (energy) |
| $\boldsymbol{X} = (\tilde{\mathbf{r}}, \tilde{\mathbf{p}})$ | = | spacecraft position and momenta in rotating, body-fixed Vesta centered frame |
| $\boldsymbol{F(X)}$ | = | associated (Hamiltonian) vector field |
| $J(\tilde{\mathbf{r}}, \dot{\tilde{\mathbf{r}}})$ | = | first integral of motion for the Vesta orbiter dynamics in terms of position and velocity |
| $P_1, P_2, P_3, P_4$ | = | relative equilibria of the orbiter dynamics |
| $\mathrm{Spec}\, A$ | = | set of eigenvalues of matrix A |
| $\lambda^j$ | = | real part of $j^{th}$ eigenvalue |
| $\omega_p^j$ | = | imaginary part of $j^{th}$ "in-plane" eigenvalue (with small $z, p_z$ components) |
| $\omega_v^j$ | = | imaginary part of $j^{th}$ "out-of-plane" eigenvalue (with large $z, p_z$ components) |
| $\boldsymbol{Z}(h)$ | = | zero velocity surface |
| $\kappa(\vec{r}, h)$ | = | implicit function defining the zero velocity surfaces and allowable region of motion |
| $\boldsymbol{\phi}_t,\ \theta$ | = | $t$-advance mapping along a trajectory and phase along a periodic orbit |
| $D\boldsymbol{\phi}_T(\boldsymbol{X}_0)$ | = | monodromy matrix (state transition matrix after one period) of a $T$–periodic orbit with initial condition $\boldsymbol{X}_0$ |
| $\boldsymbol{V}^s, \boldsymbol{V}^u$ | = | stable and unstable eigenvectors, respectively |
| $\xi^s$, $\xi^u$ | = | displacements along the stable and unstable eigenvectors, respectively |
| $\boldsymbol{\psi}(\theta, \xi^u, \xi^s)$ | = | parametrization of a stable-unstable manifold |
| $i, j, k, k_1, k_2, m, n$ | = | arbitrary integers |

## I. Introduction

As of September 2011, NASA's Dawn mission has successfully inserted into orbit around the asteroid Vesta. Dawn's Vesta exploration plan calls for eventual transfer to the Low-Altitude Mapping orbit (LAMO) at $\sim 460$ km radius [1, 2]. The LAMO has an orbital period smaller than Vesta's rotation period, so the spacecraft must cross the 1:1 resonance between the spacecraft orbit period and Vesta's rotation period using its low-thrust propulsion system. This transfer presents a mission risk because chaotic dynamics in the region around the resonance could cause unplanned trajectory excursions that would negatively impact the mission. This study is motivated by this challenge; not to design Dawn's trajectory, but to develop a general transfer design strategy for crossing this potentially–hazardous region during future missions.

The chaotic motion associated with resonant orbit dynamics results from a repeating system configuration that allows small or unmodelled perturbations to be amplified through repeated application. If the resonant frequency and strength are large enough, unpredictable and significant trajectory changes can occur over short time scales. The clearing away of asteroids near certain resonances with Jupiter's orbit period is a classic example of chaotic dynamics near resonance in celestial mechanics ([3], chapter 12). When the Dawn spacecraft is in a 1:1 resonance with Vesta, the irregular and largely–unknown gravitational potential of Vesta will repeat its influence on the Dawn spacecraft every $5.342$ hr [4]. Small variations in spacecraft state and gravitational potential can make the difference between the orbit being pushed to higher or lower altitudes, or even different orbit planes within a few days to a week [22]. It may not be possible or practical to directly counter these effects using Dawn's low-thrust engine. Tricarico and Sykes [5] have indeed shown through the numerical propagation of an assumed Vesta gravity field that a spacecraft with low thrust engines equivalent to Dawn could be delayed and miss its encounter with Ceres. The resonant nature of these phenomena has been further clarified and globally analyzed using averaging techniques in Delsate [6]. However, the periodic orbits and invariant manifolds associated with these resonances has not been analyzed. Such a viewpoint complements these approaches (point integration and semi-analytical) by providing finer details and control on the orbit structure in a particular region of phase space. This paper focuses on this approach for the case of the 1:1 resonance.

The strategy presented here is thus to follow the stable (on ingress) and unstable manifolds (on egress) of unstable, near-synchronous, periodic orbits across the chaotic region near the 1:1 resonance with Vesta's

rotation. The manifold structure of these periodic orbits defines the boundaries (locally) between approaching ballistic trajectories that successfully cross the resonance and those that do not. The stable manifolds allow definition of a set of approach states and the unstable manifolds are used to predict the post-transfer states. This approach is similar to the widely-studied use of invariant manifolds of the unstable libration orbits in the three-body problem to achieve low-energy transfers between primaries [7–9] and the use of stable manifolds to approach a desirable science orbit in the strongly perturbed environment near planetary moons [10]. Here, unstable periodic orbits in the surface-fixed rotating frame of an asteroid provide the manifold structure for the transfer design. The first family of transfers discussed arises from horizontal and vertical libration orbits near the unstable equilibrium points of Vesta. The second family of transfer opportunities presented uses near-polar unstable orbits to provide high-inclination transfers across the resonant region. Though stable-unstable manifolds are used here to design transfers across the 1:1 resonance, the approach is also applicable to designing other types of transfers throughout the gravity-dominated regime around any body with a non-spherical gravitational potential.

In this way, this paper contributes to the study of small body orbiter mission design and demonstrates that the known results about the structure of the 1:1 resonance near planets (such as the geostationary belt, e.g. [11] p. 54), persist in the largely perturbed gravity field of a particular asteroid of interest. It is shown notably that the analysis of these dynamics through the notion of periodic orbit family and associated stability analysis allows for the inclusion of higher order terms, which is in contrast with previous semi-analytical studies, which generally provide qualitative understanding based on averaging methods. The results in this paper also complement previous studies in ideal gravity fields [12] that showed the generic existence of equilibria in the 1:1 resonance region for orbiters around ellipsoid-shaped small bodies.

This paper proceeds as follows: after a review of the basic modeling and a brief elaboration on the relevant dynamical notions, the equilibria in the surface-fixed frame of Vesta and the energy constraints associated with motion near the 1:1 resonance region are described. The dynamics near the two unstable equilibria has two oscillatory components plus a hyperbolic one, which implies the existence of two nearby families of periodic libration orbits that have invariant stable and unstable manifolds. These orbits and their invariant manifolds are described, which shows that low-inclination, low-energy, transit orbits across the 1:1 resonance can be achieved ballistically by a proper approach along the stable manifold. Next, a family

of near-polar unstable orbits and their manifolds are similarly developed to show the possibilities for high-inclination transfers that may be more appropriate for a mapping mission like Dawn. The paper concludes with a discussion on how to create an end-to-end transfer trajectory using this theoretical framework and presents a few examples of transfers.

## II. Dynamic Background

This section reviews the dynamical model used for this study and the underlying simplifications. Also, a review of the notion of resonance and associated rotating frames are provided for completeness. Further discussion of resonant motion can be found in Reference [3] chapters 4,6,9,10,12 or in the research papers indicated in the introduction.

### A. Vesta Environment Modeling

The results given in this paper assume a spacecraft in orbit around the asteroid Vesta. Figure 1 provides various views of Vesta and its relative size as compared to the Moon and Ceres. Vesta is one of the largest objects in the main asteroid belt. Its principal radii measure roughly $289 \times 280 \times 229\mathrm{km}$ [13] with departures of $15$ to $20\mathrm{km}$ from a smooth ellipsoidal shape at a large crater near the south pole [14]. Because Vesta represents a large asteroid, this paper's focus is on orbit dynamics in the gravity-dominated region near a massive small body with an arbitrary gravitational potential. The two-body equations of motion in a surface-fixed, rotating coordinate frame are appropriate for the study of these dynamics, since third-body forces and solar radiation pressure (assuming typical spacecraft mass-to-area ratios) have minimal effect on motion in close-proximity to Vesta over the time scales considered. When applying this type of analysis to motion near other asteroids, it is important to verify that third-body effects are indeed small enough to ignore.

Table 1 gives the values of the parameters used here to define spacecraft motion near Vesta. In particular, Vesta is assumed to be rotating uniformly around a constant direction in inertial space and the gravitational field is modeled via spherical harmonics, as described in the Appendix. Note that fairly large gravitational field coefficients are found even at higher degree and order, which reflect the highly perturbed gravity field expected at Vesta, and distinguish this study from the classic planet orbiter case.

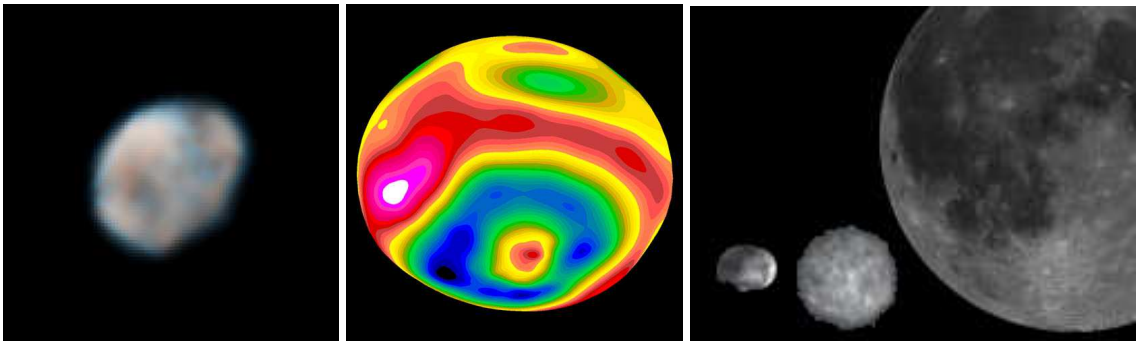

**Fig. 1 Left: image of Vesta as taken from Hubble space telescope; Middle: elevation map of Vesta showing the large southern crater and strong asymmetry of the mass distribution (elevation ranges from $-12$ km –black/blue color– to $+12$ km –red/white color) ; Right: size comparison of Vesta with Ceres and the Moon. While significantly smaller than these larger bodies, Vesta is among the largest of the asteroids (photos courtesy of NASA/ESA).**

**Table 1 Parameters for the Vesta model.**

| Parameter | Vesta | units |
|---|---|---|
| Gravitational parameter | 17.8 | $\mathrm{km}^3/\mathrm{s}^2$ |
| Rotational period | 5.342 | hrs |
| Spherical Harmonic Gravity Coefficients | 8×8 | (See Appendix) |

### B. Orbiter Equations of Motion

Consider a coordinate frame with origin at the small-body center of mass, with $z$-axis along Vesta's poles in the direction of positive rotation, and rotating at a uniform rate $\omega$ around this axis. Denote by $\tilde{\mathbf{r}} = (x, y, z)$ the rectangular coordinates of a massless spacecraft $S$ (or particle) in this coordinate frame. If $S$ is subject only to accelerations arising from the gravitational force potential of the small body, denoted as $U$ and fully developed in the Appendix, then Eqn. (1) can be used to describe the motion of $S$,

$$\ddot{\tilde{\mathbf{r}}} + 2\left(\boldsymbol{\omega} \times \dot{\tilde{\mathbf{r}}}\right) + \boldsymbol{\omega} \times (\boldsymbol{\omega} \times \tilde{\mathbf{r}}) = \nabla U, \tag{1}$$

where $\boldsymbol{\omega} = (0, 0, \omega)^\top$ and $\nabla$ denotes gradient with respect to $(x, y, z)$. In coordinates,

$$\ddot{x} - 2\omega\dot{y} = \partial_x U_{\text{eff}} \quad ; \quad \ddot{y} + 2\omega\dot{x} = \partial_y U_{\text{eff}} \quad ; \quad \ddot{z} = \partial_z U_{\text{eff}}, \tag{2}$$

where $U_{\text{eff}} = U + \frac{1}{2}\omega^2(x^2 + y^2)$ represents the effective potential.

The above equations of motion can be stated in Hamiltonian form, which is used for the numerical integrations performed in this paper. These first–order differential equations of motion are

$$\begin{aligned} \dot{x} &= dH/dp_x, \qquad \dot{y} = dH/dp_y, \qquad \dot{z} = dH/dp_z, \\ \dot{p}_x &= -dH/dx, \qquad \dot{p}_y = -dH/dy, \qquad \dot{p}_z = -dH/dz, \end{aligned} \tag{3}$$

where the Hamiltonian is

$$H(\tilde{\mathbf{r}}, \tilde{\mathbf{p}}) = \frac{1}{2}(p_x^2 + p_y^2 + p_z^2) + \omega(yp_x - xp_y) - U, \tag{4}$$

and momenta $\tilde{\mathbf{p}} = (p_x, p_y, p_z)$ are related to velocities through

$$p_x = \dot{x} - \omega y, \quad p_y = \dot{y} + \omega x, \quad p_z = \dot{z}. \tag{5}$$

The Hamiltonian is an integral of motion of Eqn. (3), hence through the relations in Eqn. (5) is also an integral of Eqn. (1). In analogy with the Jacobi constant of the circular restricted three–body problem, an integral of motion for Eqn. (1) can be deduced directly in terms of positions and velocities as

$$J(\tilde{\mathbf{r}}, \dot{\tilde{\mathbf{r}}}) = \frac{1}{2}(\dot{x}^2 + \dot{y}^2 + \dot{z}^2) - U_{\mathit{eff}}. \tag{6}$$

Actually, $H(\tilde{\mathbf{r}}, \tilde{\mathbf{p}}) = J(\tilde{\mathbf{r}}, \dot{\tilde{\mathbf{r}}})$, and because of this fact it is customary to denote the value of the Hamiltonian as "energy". This convention will be followed in the remaining of the paper. The $J(\tilde{\mathbf{r}}, \dot{\tilde{\mathbf{r}}})$ notation is kept in order to make explicit the dependence in the velocity vector for the zero-velocity discussion of the next section.

Denoting $\boldsymbol{X} = (x, y, z, p_x, p_y, p_z)^\top$, the system of differential equations given in Eqn. (3) can then be written in compact form as

$$\dot{\boldsymbol{X}} = \boldsymbol{F}(\boldsymbol{X}). \tag{7}$$

### C. Resonant Dynamics

Resonance occurs whenever two frequencies associated with the dynamics are linearly dependent over the set of integers. In our case, the basic frequencies of the equations of motion are the angular velocity of the frame, $\omega$ and the mean motion of the orbiter, $n$. Thus, if the initial conditions of the spacecraft are such that $k_1\omega - k_2 n = 0$ (where $k_1$ and $k_2$ are non-zero integers), $k_1 : k_2$ resonant motion results. Since the mean motion of the spacecraft is not constant here because of the high-order gravity terms, one

has to understand this relation in an approximate sense (i.e., for initial conditions close to exactly resonant conditions). Physically, when an orbiter is near a $k_1 : k_2$ resonance, the spacecraft performs $k_1$ orbits in inertial space while the body rotates (about) $k_2$ times around its pole.

In the case of a $1 : 1$ resonance, the orbital period of the spacecraft is nearly equal to that of the pole rotation. In the case of an Earth orbiter, this is a geosynchronous satellite. In the unperturbed two-body case, the geostationary belt is a continuous set of equilibria relative to the Earth surface, which correspond to circular orbits with zero inclination and periods of one sidereal day. This fact comes from axial symmetry, and would also apply e.g. to a zonal mode. Back in the point-mass Earth orbiter case, deviation in inclination leads to closed "figure-eight" ground tracks and periodic orbits in an Earth-centered-fixed frame. Similarly, changes in eccentricity lead to in-plane periodic orbits centered at the geostationary equilibria. Finally, small changes in period lead to small drifts of the ground track.

In the case of a non-pointmass gravitational potential, this idealized picture is modified, so that small changes in semi-major axis do not necessarily lead to drift from the equilibria. In fact, several types of motion can be observed, ranging from small librations about the ideal geostationary location to small constant drifts in the along-track direction moving away from the desired geostationary point. As Kaula reviewed in [11], section 3.6, these motions are due to the presence of stable and unstable equilibria, mostly dominated by the $C_{22}$ term. For more irregular bodies like Vesta and other asteroids, the types of motion near the 1:1 resonance are similar, but more pronounced and potentially occurring over a much shorter timescale [12].

Because of all this rich dynamical structure (that, in the following sections, will be found magnified with respect to Earth's geostationary belt) it is difficult to give a precise mathematical definition of the "resonant region" as a particular set of states. In this paper, a simple geometrical convention will be followed. The resonant region will be considered as the set of states with $\tilde{\mathbf{r}}$ within a few $\mathrm{km}$ of the two–body point-mass resonant radius, $(\mu/\omega^2)^{1/3}$.

### III. Relative Equilibria and Energy Constraints

Following the general comments of the previous section, the equilibria associated with 1:1 resonant dynamics are computed in the particular case of Vesta. This section follows the approach of Scheeres [12], which identified relative equilibria near an ellipsoid model of Vesta, noted the existence of nearby orbits,

and discussed the local zero-velocity surfaces. The presentation given here emphasizes the features relevant to transfers that use the manifolds of the unstable resonant orbits with an $8 \times 8$ gravity model of Vesta. As mentioned in the introduction, the demonstration of the applicability of dynamical systems theory to analyze these dynamics with a given complex gravity field is one of the contributions of this paper.

### A. Relative Equilibria Solutions

Relative equilibria, that is, equilibrium solutions for the equations of motion expressed in the rotating frame, are a special case of 1:1 synchronous orbits where the orbiting spacecraft presents a fixed location relative to the body surface at all times. They generally lie near the equatorial plane, because the $z$ component of $\nabla U$ must be zero (see Eqn. 2), and roughly $\left(\mu/\omega^2\right)^{1/3}$ away from the center of mass. If the gravitational potential is axially-symmetric about $\hat{\mathbf{z}}$, a continuum of equilibria encircle the body. In the case of an irregular gravitational potential, there are usually $4$ equilibria [11, 12], though for certain body shapes there may exist more [15].

Equilibria near Vesta are computed by solving $\nabla U_{\mathit{eff}} = 0$. This can be done using a standard Newton-Raphson iteration scheme, with initial guesses down-selected from a grid survey of the function value in the resonance region, as shown in Fig. 2. The location of the computed equilibria are given in Table 2. For increasing longitudes, these solutions are labeled as $P_1$, $P_2$, $P_3$, $P_4$. They are found to lie in different horizontal planes within a few $\mathrm{km}$ of the equator.

**Table 2 Coordinates of the fixed points in rotating coordinates**

| Point | $x$ (km) | $y$ (km) | $z$ (km) | $\lambda$ (deg) | $\phi$ (deg) | Stability | Energy ($\mathrm{km}^2/\mathrm{s}^2$) |
|---|---|---|---|---|---|---|---|
| $P_1$ | 499.979 | 247.022 | $-1.464$ | 26.29 | $-0.15$ | unstable | $-0.048933$ |
| $P_2$ | $-202.948$ | 515.982 | 0.170 | 111.47 | 0.02 | stable | $-0.048745$ |
| $P_3$ | $-521.602$ | $-196.344$ | $-1.001$ | 200.63 | $-0.10$ | unstable | $-0.048917$ |
| $P_4$ | 198.838 | $-517.908$ | $-1.381$ | 291.00 | $-0.14$ | stable | $-0.048758$ |

Of these $4$ points, the linear behavior around $P_2$ and $P_4$ is completely oscillatory, whereas $P_1$ and $P_3$ have hyperbolic parts. Using the nomenclature of Scheeres [12], Vesta can be considered a "Type 1" body.

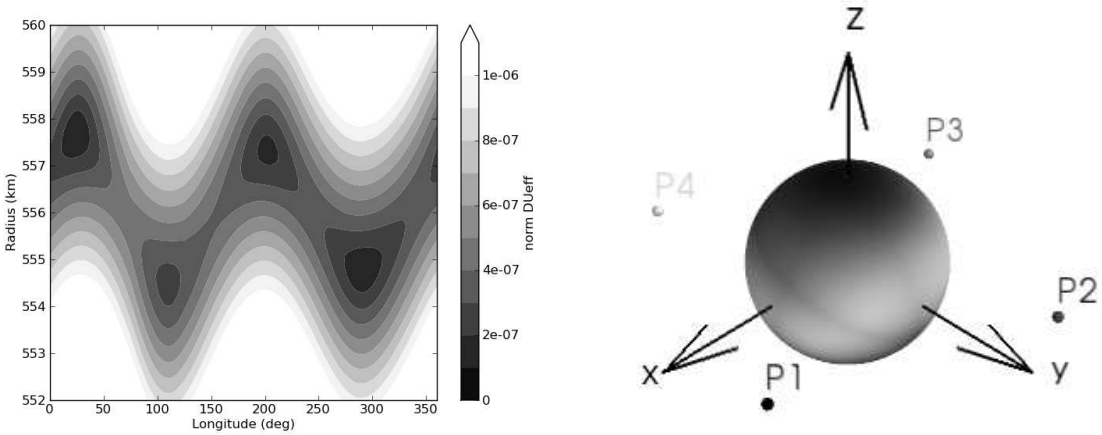


**Fig. 2 Left: For the values of radius and longitude represented, minimization of $\|\nabla U_{eff}\|$ for latitude between $-10$ and $10$ degrees. Right: Gravitational force potential value on $260$ km sphere with location of the relative equilibria; darker colors represent lower effective potential $U_{eff}$ values, illustrating the asymmetry of Vesta gravitational field.**

Namely, the sets of eigenvalues (denoted *Spec*) of the linearized dynamics $D\boldsymbol{F}$ are given as:

$$\begin{aligned} j &= 1,3, \qquad \operatorname{Spec} D\boldsymbol{F}(P_j) = \{\pm\lambda^j, \pm i\omega_p^j, \pm i\omega_v^j\}, \\ k &= 2,4, \qquad \operatorname{Spec} D\boldsymbol{F}(P_k) = \{\pm i\omega_1^k, \pm i\omega_2^k, \pm i\omega_3^k\}. \end{aligned} \tag{8}$$

In the unstable equilibria cases of $P_1$ and $P_3$, there are eigenplanes that are close to planar ($z, p_z$ components small compared to $x, y, p_x, p_y$) and close to vertical ($x, y, p_x, p_y$ components small compared to $z, p_z$). The corresponding pairs of complex conjugate eigenvalues have been denoted as $\pm i\omega_p^j$ and $\pm i\omega_v^j$, respectively. Numerical values are given in Table 3.

**Table 3 Eigenvalues of the fixed points in Eqn. (8)**

| $j$ | $\lambda^j$ | $\omega_p^j$ | $\omega_v^j$ | $k$ | $\omega_1^k$ | $\omega_2^k$ | $\omega_3^k$ |
|---|---|---|---|---|---|---|---|
| 1 | $6.27114 \times 10^{-5}$ | $3.21174 \times 10^{-4}$ | $3.38038 \times 10^{-4}$ | 2 | $6.53482 \times 10^{-5}$ | $3.10428 \times 10^{-4}$ | $3.35938 \times 10^{-4}$ |
| 3 | $5.91673 \times 10^{-5}$ | $3.21221 \times 10^{-4}$ | $3.37354 \times 10^{-4}$ | 4 | $5.56534 \times 10^{-5}$ | $3.11893 \times 10^{-4}$ | $3.36326 \times 10^{-4}$ |

In order to give an idea about how all the dynamical structure that will be computed in the following section relates to simpler models, Tables 4,5 show the location of the four fixed points $P_1, \ldots, P_4$ for truncation to order and degree 2 and 3, respectively, of the spherical harmonic expansion described in the Appendix. Since the difference in radius with respect to the full $8 \times 8$ model is under $1\,\mathrm{km}$, a reasonable guess is that the whole structure would be displaced in longitude in values similar to the ones shown in these Tables.

**Table 4 Coordinates of the fixed points in rotating coordinates for the truncation of the spherical harmonic model to degree and order 2. The difference in radius, longitude and latitude with respect to the full $8 \times 8$ model is also shown. The units are $\mathrm{km}$ for $x, y, z, r$, and $\mathrm{deg}$ for $\lambda, \phi$.**

| Point | $x$ | $y$ | $z$ | $r - r_{8\times8}$ | $\lambda - \lambda_{8\times8}$ | $\lambda - \lambda_{8\times8}$ |
|---|---|---|---|---|---|---|
| $P_1$ | 513.037 | 217.356 | 0.120 | $-0.494$ | $-3.33$ | 0.16 |
| $P_2$ | $-216.249$ | 510.422 | 0.651 | $-0.118$ | 1.49 | 0.05 |
| $P_3$ | $-513.037$ | $-217.356$ | $-0.120$ | $-0.152$ | 2.33 | 0.09 |
| $P_4$ | 216.249 | $-510.422$ | $-0.651$ | $-0.426$ | 1.96 | 0.08 |

**Table 5 Coordinates of the fixed points in rotating coordinates for the truncation of the spherical harmonic model to degree and order 3.**

| Point | $x$ | $y$ | $z$ | $r - r_{8\times8}$ | $\lambda - \lambda_{8\times8}$ | $\lambda - \lambda_{8\times8}$ |
|---|---|---|---|---|---|---|
| $P_1$ | 503.268 | 239.534 | $-0.918$ | $-0.309$ | $-0.84$ | 0.06 |
| $P_2$ | $-217.165$ | 509.888 | 0.260 | $-0.252$ | 1.60 | 0.01 |
| $P_3$ | $-523.025$ | $-191.621$ | $-1.174$ | $-0.310$ | $-0.51$ | $-0.02$ |
| $P_4$ | 214.976 | $-511.106$ | $-1.040$ | $-0.291$ | 1.81 | 0.04 |

### B. Zero-velocity surfaces

Additional insight into the dynamics near the 1:1 resonance of Vesta is gained by studying the zero-velocity surfaces near the equilibria. Using the integrals of the dynamics given in the previous section (Eqns. (4), (6)), a surface in position space can be defined for a given energy level $J(\tilde{\mathbf{r}}, \dot{\tilde{\mathbf{r}}}) = h$ which a spacecraft with this energy cannot cross without achieving a complex velocity vector (impossible). More formally, the zero-velocity surface $\mathbf{Z}(h)$ is defined as $\mathbf{Z}(h) = \left\{\tilde{\mathbf{r}} \in \Re^3 \quad | \quad \kappa(\tilde{\mathbf{r}}, h) = J\left(\tilde{\mathbf{r}}, \tilde{\mathbf{0}}\right) - h = 0\right\}$ where $h = H(\tilde{\mathbf{r}}, \tilde{\mathbf{p}}) = J(\tilde{\mathbf{r}}, \dot{\tilde{\mathbf{r}}})$ is the energy of the spacecraft. Motion is energetically permitted at $\tilde{\mathbf{r}}$ when $\kappa(\tilde{\mathbf{r}}, h) < 0$ and is not otherwise.

By computing the value of $J\left(\tilde{\mathbf{r}}, \tilde{\mathbf{0}}\right)$ on a grid of positions near the equilibria, the structure of the local zero–velocity surfaces for different energies can be visualized. Figures 3(a)-(c) show contours of $J\left(\tilde{\mathbf{r}}, \tilde{\mathbf{0}}\right)$ on

various surfaces in position space. For a spacecraft with a particular energy value, positions having lighter colors are inaccessible, while darker colored regions are not restricted energetically. The projection of the equilibrium locations are shown on the plots as well.

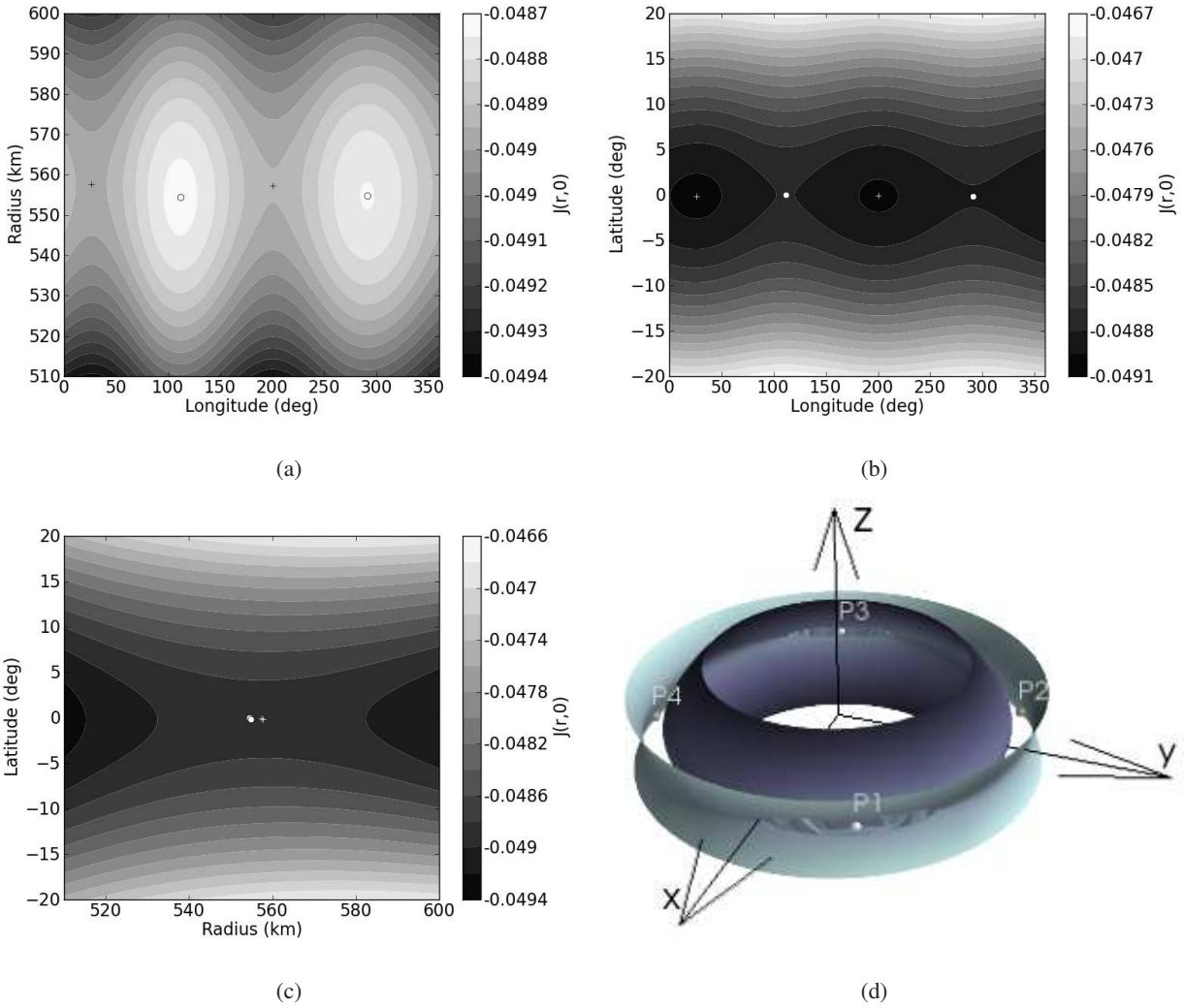


**Fig. 3 Contours of zero–velocity surfaces $J(\tilde{\mathbf{r}}, \tilde{\mathbf{0}})$, with units $\mathrm{km}^2/\mathrm{s}^2$, in (a) the equatorial plane (latitude fixed at $0$ deg), (b) out of plane near the 1:1 resonance at Vesta (radius fixed at $555$ km) and (c) in the vertical plane (longitude fixed at $0$ deg). The projected locations of the stable equilibria are shown as small white disks, while the unstable equilibria are represented as small crosses. Given an initial energy value, future motion is only allowed in the regions with smaller values of $J(\tilde{r}, 0)$ (darker colors). Plot (d) shows a 3-dimensional, cut-out view of the zero velocity surfaces near the equatorial plane at $J = -0.0489$, to illustrate the topology of the opening near the unstable equilibria, $P_1$ and $P_3$.**

In Figure 3(a), the two stable equilibria, $P_2$ and $P_4$, reside at local maxima of $J\left(\tilde{\mathbf{r}}, \tilde{\mathbf{0}}\right)$. Thus, a spacecraft

starting with zero velocity at $P_2$ or $P_4$ is not restricted energetically from moving anywhere in the equatorial plane. However, as indicated in the previous section, these equilibria are stable and the motion is actually *dynamically constrained* to stay within the neighborhood of the these points (over very long times scales).

Conversely, the unstable equilibria, $P_1$ and $P_3$, are at saddle points of the zero velocity surface. For energies slightly larger than these critical values, a spacecraft starting at one of these points is constrained to move mostly radially inward or outward. These energies are the minimum ones at which transit through the resonance is possible. Figure 3(d) illustrates this situation in a 3-dimensional representation of a section of the zero-velocity surface. It is in essence similar to low energy ballistic transfers between the two primaries in the circular restricted three-body problem [7]. Note, in particular, that the energy value at $P_1$ is smaller than $P_3$, implying that *transit through the 1:1 resonance is possible first through* $P_1$, *when* $J > -4.8932 \times 10^{-2}\,\mathrm{km}^2/s^2$.

The energy constraints can also give rough estimates of some properties of the transfers at low energies. For example, it can be observed that the radius along a given zero velocity surface decreases (resp. increases) when moving toward $P_2$ and $P_4$ along the side of the surface closer to (resp. farther from) Vesta. The difference between the extrema in radius along the zero velocity surface provide a good estimate of the change in semi-major axis to be expected when crossing the resonance at these low energies. From Fig. 3(a), this change can thus be expected to be greater than $60\ \mathrm{km}$. As we will see, these estimates provide good lower bounds on the results based on invariant manifold computations presented in the next section at these energies. For larger energy values, however, the constraint is not energetic, but rather dynamic in nature, and the manifold computations are then necessary.

From Figure 3(b), one can notice also that $J\left(\tilde{\mathbf{r}}, \tilde{\mathbf{0}}\right)$ increases as latitude moves away from zero, showing that ballistic crossing with low energies must occur near the equatorial plane, with low inclinations (the inclination of a state on a zero velocity surface is equal to the latitude at that position). Fig. 3(c), however, indicates that inclination is not constrained as one gets closer to Vesta. There again, dynamical constraints represented by the manifolds associated with transit trajectories provide the dynamical barriers that keep, in actuality, the motion near to equatorial orbits at these energies. A good estimate of the range of inclinations of these transit orbits at low energies is given by the size of the opening in latitude at $P_1$ and $P_3$. In any case, for highly inclined resonant crossing transfers, as desirable for a global-mapping mission like Dawn, one

requires larger energies and the computation of dynamical constraints as captured by the notion of manifolds associated with unstable periodic orbits.

## IV. Resonant Periodic Orbits and Associated Manifolds

Lyapunov's center theorem ensures that, for a fixed point of a Hamiltonian vectorfield, and under suitable non–resonance conditions among eigenvalues, the families of periodic orbits of the linear approximation that lie in the eigenplanes corresonding to conjugated, purely imaginary eiganvalues become (in the full, non–linear system) families of p.o. with varying periods that span 2D manifolds tangent to the corresponding eigenplane of the fixed point (see e.g. [16] p. 156). In our case, for each pair of purely imaginary, complex conjugated eigenvalues of $D\boldsymbol{F}(P_i)$, $i = 1, 3$, a family of periodic orbits is generated that fills a two–dimensional manifold tangent to the corresponding eigenplane at the fixed point. The families generated from the $\pm i\omega_p$ eigenplanes will be denoted as planar Lyapunov families, whereas the ones corresponding to the $\pm i\omega_v$ will be denoted as vertical Lyapunov families. Their study is the subject of the following section, together with some families of near-circular, near-polar orbits that, in the case of Vesta, appear as disconnected from the Lyapunov families.

In all the descriptions of families of periodic orbits that will follow, energy will be used as the parameter identifying a particular orbit of the family. Linear stability will be described in terms of the stability index introduced by Hénon[17]. Namely, given an initial condition $\boldsymbol{X}_0$ of a periodic orbit of period $T$, denote the eigenvalues of its monodromy matrix (state transition matrix after one period) as

$$\mathrm{Spec}\, D\boldsymbol{\phi}_T(\boldsymbol{X}_0) = \{1, 1, \Lambda_1, 1/\Lambda_1, \Lambda_2, 1/\Lambda_2\}$$

(the fact that the eigenvalues appear as above is a consequence of the fact that the differential equations are Hamiltonian, see e.g. [16] page 48 Theorem 3.1.3, page 57 Proposition 3.3.1, and page 200 Lemma 8.5.5). The stability index associated to a pair of inverse eigenvalues $\Lambda_j$, $1/\Lambda_j$ is defined as

$$s_j = \Lambda_j + 1/\Lambda_j.$$

Denote eigenvectors of $\mathrm{Spec}\, D\boldsymbol{\phi}_T(\boldsymbol{X}_0)$ of eigenvalues $\Lambda_j, 1/\Lambda_j$ by $\boldsymbol{U}_j, \boldsymbol{V}_j$ respectively. For real $s_j$ with $|s_j| > 2$, the p.o. has stable and unstable manifolds tangent to $\boldsymbol{U}_j, \boldsymbol{V}_j$ (it is customary to speak of a "saddle" component of the normal behavior to the periodic orbit). For real $s_j$ with $|s_j| < 2$, the p.o. has invariant tori

around it that can be approximated linearly from the real and imaginary parts of $\boldsymbol{U}_j$ (it is usual to speak of a "center" component in this case). The case in which $s_j$ is complex is known as "complex saddle", and does not take place in any of the families of p.o. computed in this paper. See e.g. [18] for additional details and formulae.

All the numerical integrations performed for the results presented in the remaining of the paper have been done in double precision and physical units (space in $\mathrm{km}$, time in $\mathrm{s}$). The integration method used has been a variable-step RKF78 one with a relative tolerance of $10^{-14}$. In the evaluation of the vectorfield of Eqn. (3), Cunningham's recurrences [19] are used in the computation of $\nabla U$ and $\mathrm{Hess}\, U$. All the periodic orbits computed are numerically periodic within an absolute tolerance of $10^{-10}$.

### A. Families originating from relative equilibria

The planar and vertical Lyapunov families around the points $P_1$ and $P_3$ have been numerically continued, starting from the linear approximation in the corresponding eigenspaces of $D\boldsymbol{F}(P_1)$ and $D\boldsymbol{F}(P_3)$. For all the families, the continuations have been stopped at collision with the reference sphere of the Vesta spherical harmonic gravity model at $258\mathrm{km}$ radius. Some sample orbits of each family are displayed in Fig. 4. The motion in all of them is retrograde (clockwise) when projected in the equatorial plane as seen from above.

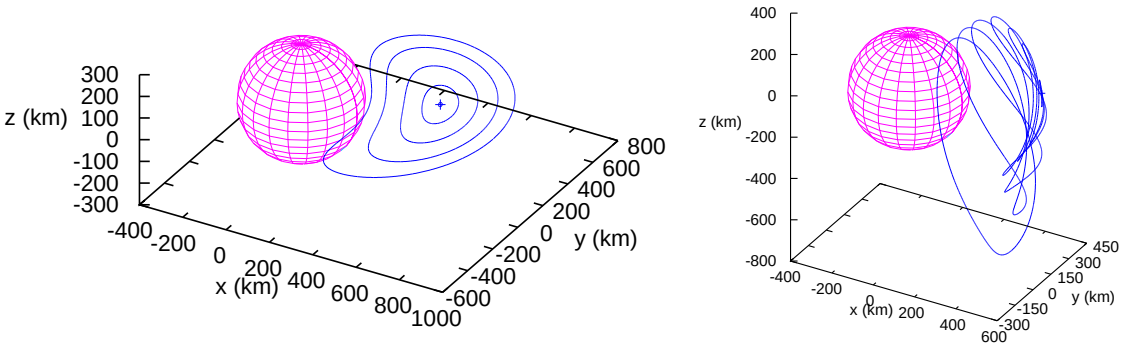


**Fig. 4 Sample orbits of the planar Lyapunov family (Left) and vertical family (Right) around $P_1$. At the scale of the figure, the $P_3$ orbits appear as symmetric relative to the origin of the frame.**

The resulting characteristic curves (energy-period and energy-linear stability index) are shown in Fig. 5. Observe that the normal behavior to all of these orbits is of center $\times$ saddle type. For the vertical families, the center stability index closely approaches the value 2 (which would imply a 1:1 bifurcation) but never reaches

it. The other stability index is always smaller than $4$. This mild instability along the families indicates that ballistic transfers can be expected to be slow relative to the orbit period. In as much as these orbits are near to the 1:1 resonance with Vesta, one can expect transfers to require at least a few days to cross the resonance (that is, at least, an order of magnitude longer than the $5.342\ hr$ orbit period of Vesta).

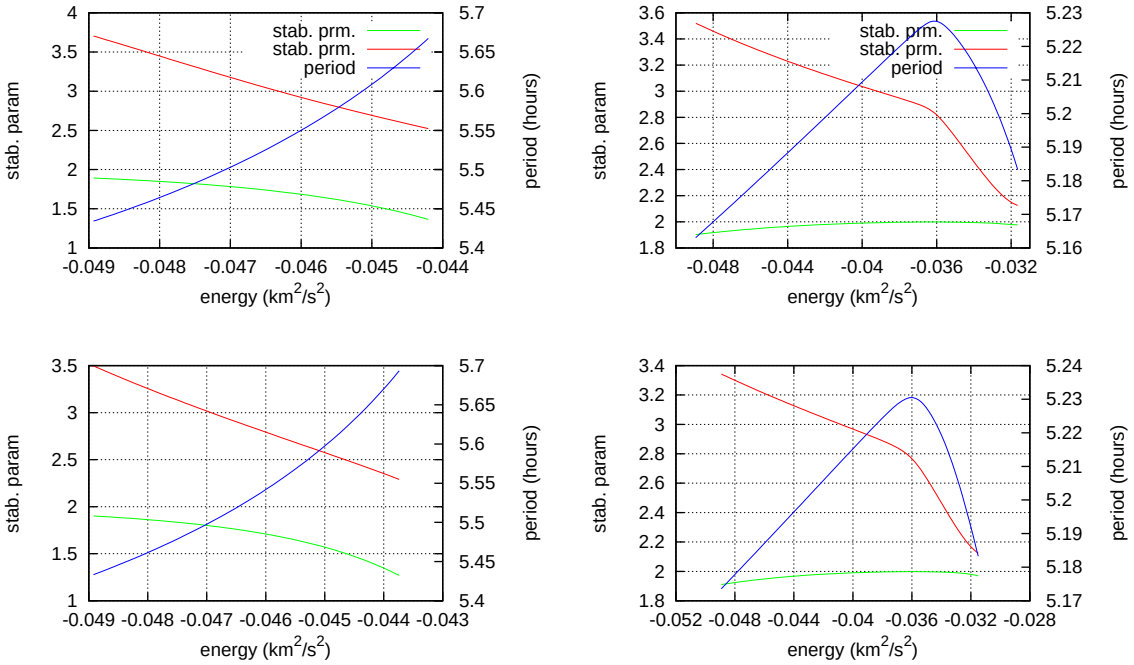


**Fig. 5 Characteristic curves (energy-period and energy-stability index) of the planar (first column) and vertical (second column) families of Lyapunov orbits around $P_1$ (first row) and $P_3$ (second row).**

Fig. 6 indicates further interesting measures of the behavior of these families. Notably, longitudinal oscillations of almost $70$ deg can be observed for the planar Laypunov families, while extrema in latitude close to $60$ deg can be observed for the near-collision vertical orbits. The sizes of these oscillations are observed in the associated manifold branches and resulting ballistic transfers computed later, as we will see in the following paragraphs. In particular, the manifold branches at large energies (and the resulting transfers) present a small eastward or westward drift superimposed on large longitudinal oscillations. The maximum latitude reached by the manifold branches is also of the same order of magnitude as the associated periodic orbits, showing that the vertical family cannot lead to truly polar orbits.

The invariant manifolds of both the vertical and planar Lyapunov families of $P_1$, $P_3$ reproduce qualitatively the behavior in the geostationary belt described in standard references (e.g. [11] p. 54). This fact is illustrated in Fig. 7 left, in which the manifolds of the planar orbit act as separatrices between libration mo-

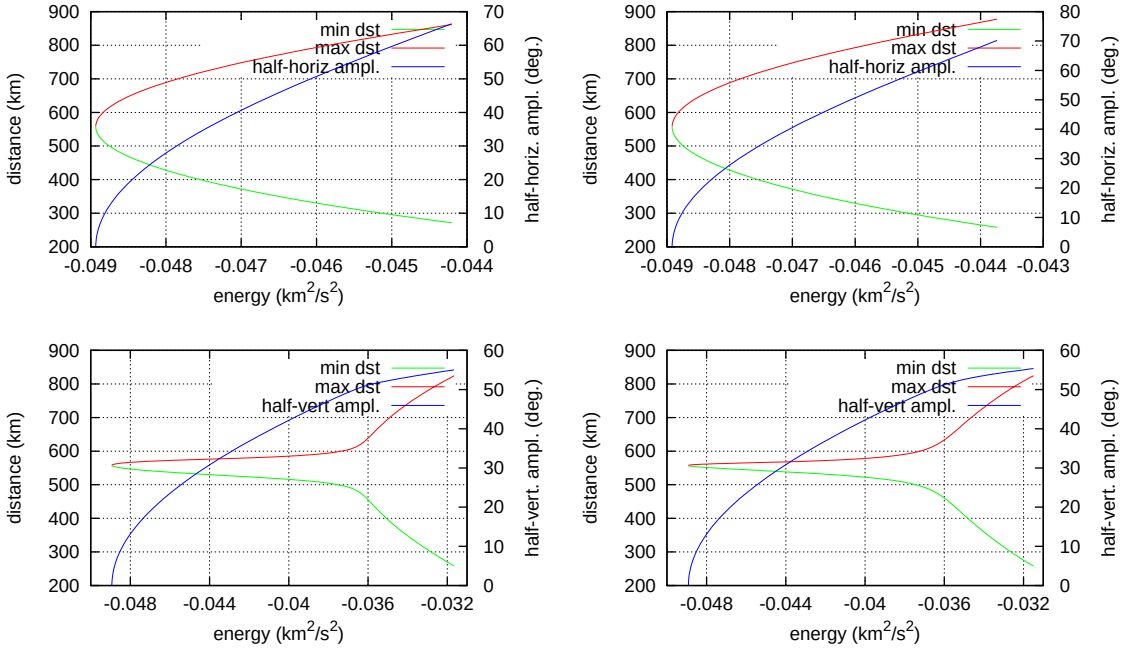


**Fig. 6 First row: Longitudinal amplitudes and extrema in radii reached along the planar Lyapunov families. Second row: Maximum latitude and extrema in radii reached along the vertical families. The left column corresponds to the families originating from the $P_1$ equilibrium solution, while the right one corresponds to the $P_3$ case.**

tion around the points $P_1$, $P_3$, and circulation motion around Vesta both inside and outside the 1:1 resonant zone. Since both the planar and vertical Lyapunov families grow in size up to collision with Vesta's reference sphere, the qualitative behavior of the geostationary belt is reproduced here on a larger scale (relative to body size), and involves orbits of relatively high inclination (see Fig. 7, right).

Similarly to the case of the $L_1$ libration points for transit between the two primaries in the circular restricted three-body problem, the manifolds associated with $P_1$ and $P_3$ can be used to construct 1:1 resonance crossing ballistic transfers. For either a planar or a vertical Lyapunov orbit around $P_1$ or $P_3$, by choosing a branch of the unstable manifold growing outwards and a branch of the stable one going inwards, a transfer from the exterior region to the interior region of the 1:1 resonance can be constructed, as will be demonstrated in the next section. A transfer from the inside to the outside region can also be constructed by choosing the suitable branches. Indeed, by combining manifolds of different points, a trajectory traversing the resonant region in both directions could be constructed. Near planar transfers can be obtained from planar Lyapunov orbits. Vertical transfers of different inclinations can be obtained by considering vertical Lyapunov orbits of

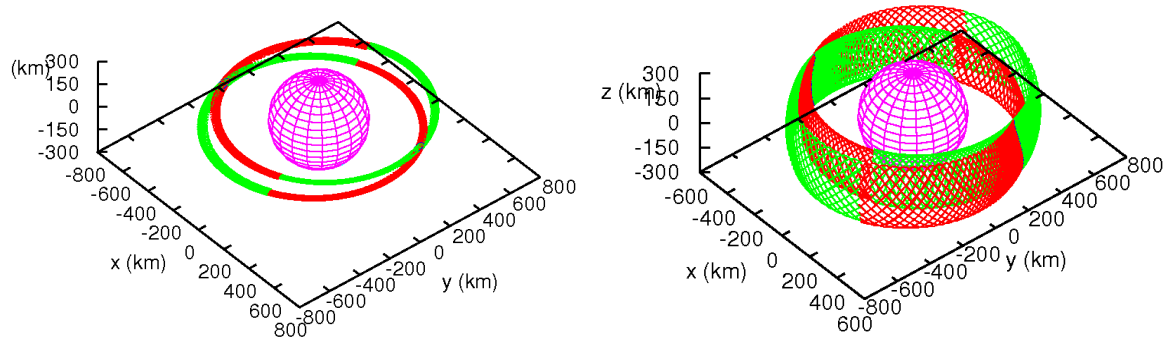


**Fig. 7 Stable (red) and unstable (green) manifold branches associated with sample Lyapunov orbits. Left: Planar family. Right: Vertical family. These plots illustrate the concept of a resonant belt bounded by the manifolds (dynamical constraints).**

different sizes. Fig. 8 illlustrates this point by displaying the branches of vertical Lyapunov orbits of different sizes allowing to construct transfers from the exterior to the interior region. In this figure, the manifold tubes have been grown up to its intersection with a meridian plane with longitude equal to the longitude of the fixed point plus 90 degrees, at which the change in semi-major axis of the trajectories on these manifolds are close to local extrema. After traversing this plane, the manifold tubes approach again (in a geostationary–like behavior as in Fig. 7) and interact with $P_3$[23]

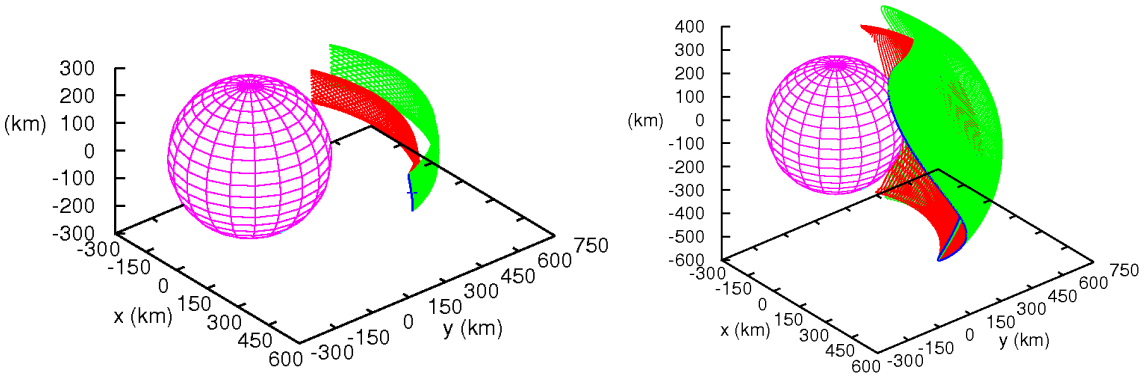


**Fig. 8 Unstable (red) and stable (green) manifold branches of sample orbits of the vertical Lyapunov families (blue curves) around $P_1$ up to a meridian plane orthogonal to the equatorial projection of the $P_1$ radius vector, at two different energies: $h = -0.048664$ km$^2$/s$^2$ (left) and $h = -0.035637$ km$^2$/s$^2$ (right). Observe the increase in inclination reached by the manifold branches as energy increases. The case of $P_3$ manifolds is symmetric relative to the origin of the frame at this scale.**

In fact, the computation of the closest/farthest approaches of the manifold tubes on these meridian planes provides a characterization of the ranges of altitude changes to be expected when crossing the 1:1 resonance using these dynamics. Fig. 9 displays the evolution of these maximum and minimum distances along the whole families (i.e. as a function of the energy value) of planar and vertical families at $P_1$ and $P_3$. Note in particular that, as the transit routes open at $P_1$ and $P_3$ near the critical energy values, the differences in periapsis and apoapsis along one manifold branch are close to zero, thus indicating that these low energy transit orbits are nearly circular. As can be seen from Fig. 9, the estimated change in semi-major axis for a 1:1 transit at these low energies appears to be on the order of $150\ \mathrm{km}$, showing the conservative nature of the lower bounds from the energy estimates (indicated in the previous section) when compared with the manifold computations.

At higher energies, the changes between the maximum and minimum altitudes between the two branches of the manifold (inner and outer) increase significantly, reaching values greater than $550\ \mathrm{km}$ and altitudes lower than $300\ \mathrm{km}$ for the planar Lyapunov orbits. While these orbits are no longer circular, they may be more interesting for space mission applications, notably as the the range of feasible transfers is larger, with options for smaller transit times, and higher inclination ranges when following manifolds of the vertical family. It should be noted, however, that the maximum range in inclination along the vertical family is still restricted and truly polar orbits cannot be reached using these manifolds. This is in constrast to nearly symmetric gravitational fields, such as the Earth. In the two-body problem, polar orbits can be continued from a family of vertical orbits. In the case of Vesta's full gravity field, the families collide with Vesta's surface before reaching polar inclinations.

### B. Families originating from polar, near-circular orbits

Given the interest of reaching polar inclination for mapping small bodies (as indicated by the Dawn mission trajectory), two distinct families of unstable resonant polar orbits were found using a differential corrector scheme with an initial guess from the two-body dynamics. One family crosses the equator near $P_1$ and the other near $P_3$ [24]. Fig. 10 provides sample orbits in these families, while Fig. 11 describes the corresponding characteristic curves and stability indices. As with the Lyapunov families, these orbits present mild instability, thus indicating time scales of several days to complete a transit.

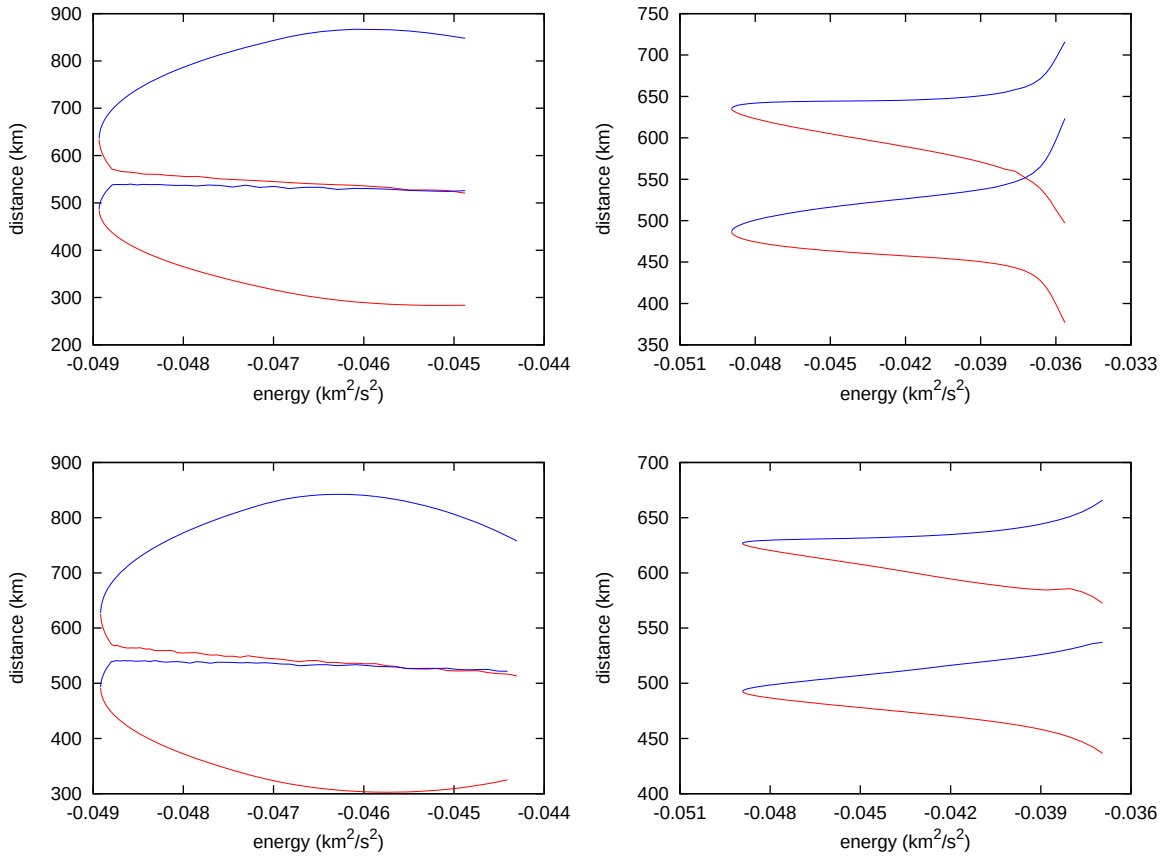


**Fig. 9 For the points $P_1$ (first row), $P_3$ (second row), and for the planar Lyapunov families (first column) and the vertical ones (second column), pericenter (red) and apocenter (blue) distances of the sections of the manifold branches allowing to construct a transfer from the exterior to the interior region of the 1:1 resonance.**

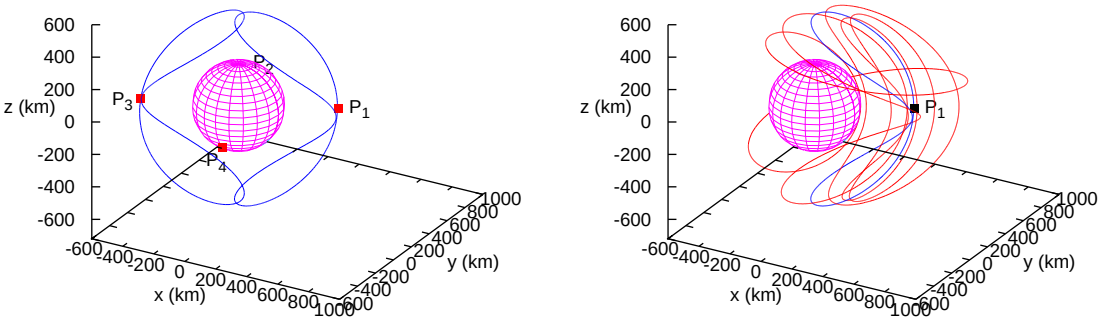


**Fig. 10 Left: 1:1 resonant unstable polar periodic orbits found from two-body initial guesses and differential correction. Right: sample orbits in the $P_1$ polar family.**

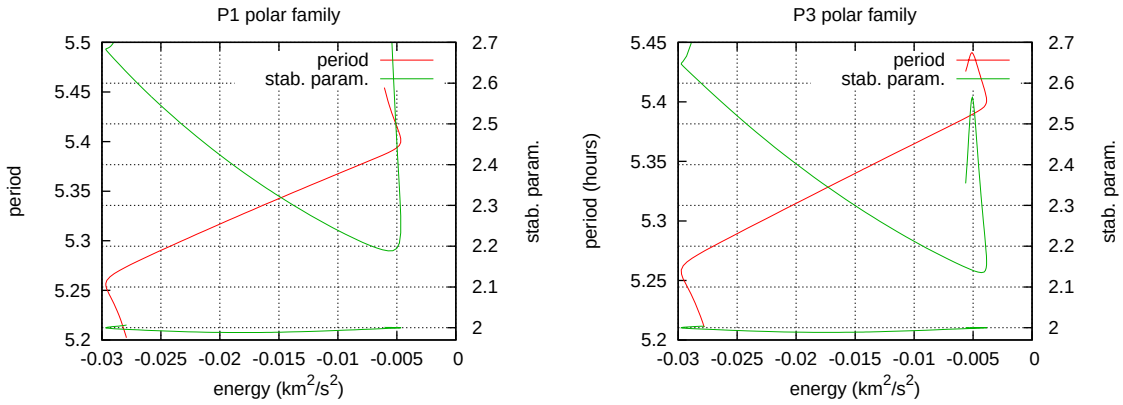


**Fig. 11 Characteristic curves and stability indices of the polar families of unstable periodic orbits wrapping around $P_1$ (left) and $P_3$ (right).**

The continuation of these families in the two possible directions ends with surface-impacting orbits, as shown in Fig. 10 (right). While the overall shape, orientation, and the corresponding situation of these orbits in a weakly perturbed two–body problem suggests that these families could be a continuation of the vertical families, these connections cannot be made in practice in this problem, and these orbits are thus considered as separate families, referred to as the "polar families"[25].

However, as for the case of the Lyapunov families, the manifolds of these orbits can be computed to provide transfer routes across the 1:1 resonance. Fig. 12 shows two manifold branches associated with a sample periodic orbit in these families, while Fig. 13 describes the extrema and changes in distance of these manifolds. These characteristics have been here computed using simultaneous crossings with the equatorial plane and the meridian plane lying +90 *deg* from the equilibria $P_1$ and $P_3$, respectively, due to the geometry of these orbits. Indeed, several members of the polar orbit families cross the meridian plane themselves, making the intersection of this plane with the manifold tubes rather ill-defined. As can be observed, reductions in altitude of over $100$ km can be obtained from the manifold tubes associated with the orbits of smaller energies.

## V. Ballistic Resonance Crossing

In this section, the notion of transit orbit is reviewed and applied to create sample 1:1 resonance crossing, ballistic trajectories near Vesta.

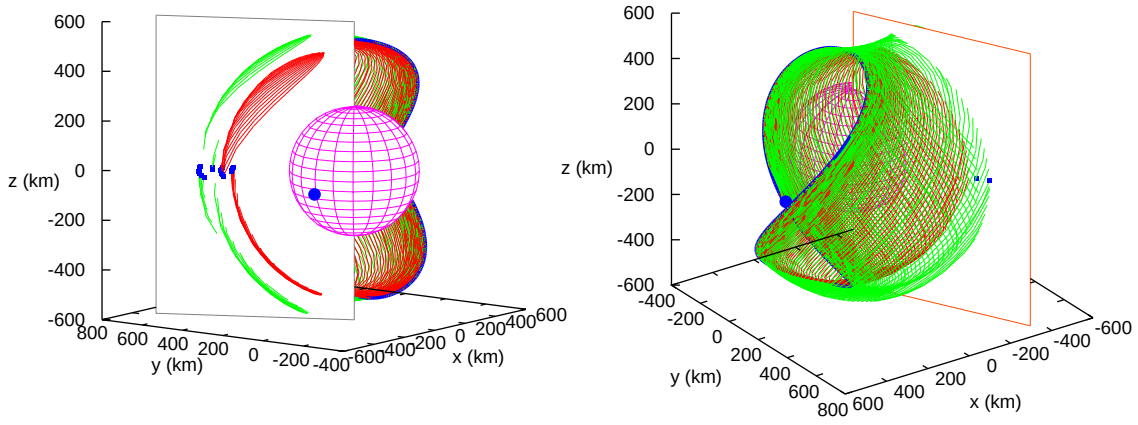


**Fig. 12 From two different viewpoints, unstable (red) and stable (green) manifold tubes of an orbit of the polar family around $P_1$. The meridian plane has been rendered as opaque to aid visualization. The thick blue curve is the p.o. The blue round points are $P_3$ (left plot) and $P_1$ (right plot). The blue square points are the first equatorial crossings of trajectories in the manifold tubes after traversing the meridial plane of the longitude of $P_1$ plus 90 *deg*.**

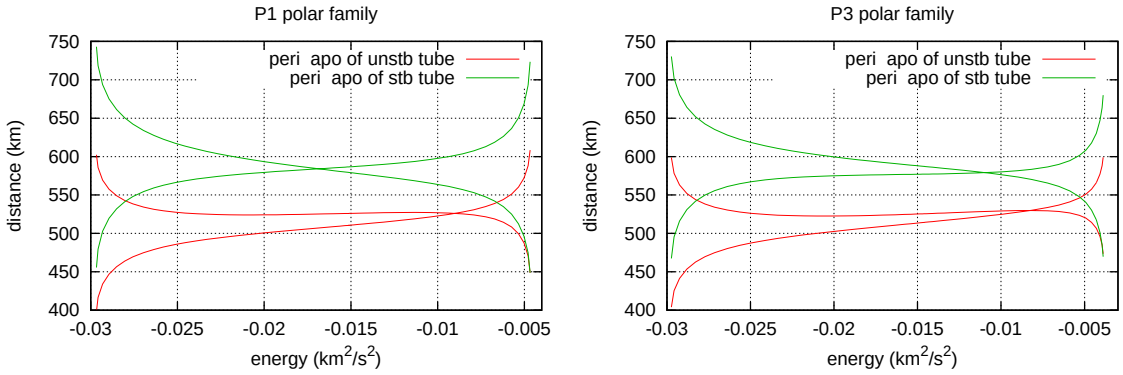


**Fig. 13 Maximum and minimum distances in an equatorial section, for the inner (red) and outer (green) manifold tubes associated with the two polar families.**

### A. Transit Orbits

In the context of the planar, restricted three–body problem, transit orbits are defined as those that traverse the orbit of the secondary around the primary from the exterior to the interior of the region of possible motion, or vice-versa. Classical works by Conley and McGehee[7, 8] have characterized them in terms of the relative position of an initial condition on a Poincaré section with respect to the section of a manifold tube of a Lyapunov orbit. By combining these characterizations with homoclinic and heteroclinic connections, later

works have been able to construct resonance transitions[9, 20].

In our case, transit trajectories will be considered as those traversing the 1:1 resonance from the outside region to the inside one. More precisely, when looking at the ground track of non-resonant orbits, the successive equatorial crossings will circulate eastward or westward. A resonant crossing trajectory will thus present a ground track that transitions between westward and eastward drifts, with a temporary turning point when crossing the resonance.

Due to the fact that we are working with a 3D gravity field, we need to consider the 4D tubes filled by the manifolds of all the periodic orbits and invariant tori at a particular energy level in order to characterize transit trajectories in terms of manifolds [20]. Although they can be computed, there is still the difficulty of the determination of the interior and exterior of the 3D intersection of these manifold tubes with a Poincaré section.

A way to produce transit trajectories from the families of periodic orbits computed in this paper is to take initial conditions in a specific quadrant of the stable/unstable eigenplane of the monodromy matrix of the periodic orbit. This quadrant has to be chosen such that, when integrating both forward and backward in time, the resulting trajectory closely follows the manifold branches of Fig. 8. To do this, assume that $\boldsymbol{X}_0$ is an initial condition of a planar or vertical Lyapunov periodic orbit with

$$\operatorname{Spec} D\boldsymbol{\phi}_T(\boldsymbol{X}_0) = \{1, 1, \Lambda, 1/\Lambda, e^{i\omega}, e^{-i\omega}\}$$

for $\Lambda > 1$, where $D\boldsymbol{\phi}_T(\boldsymbol{X}_0)$ is the monodromy matrix of the periodic orbit (state transition matrix after one period). Denote $\Lambda^u = \Lambda$, $\Lambda^s = 1/\Lambda$, consider $\boldsymbol{V}^u$ a unitary eigenvector of eigenvalue $\Lambda^u$ of $D_T\boldsymbol{\phi}(\boldsymbol{X}_0)$, and $\boldsymbol{V}^s$ a unitary eigenvector of eigenvalue $\Lambda^s$. Then,

$$\boldsymbol{\psi}(\theta, \xi^u, \xi^s) = \boldsymbol{\phi}_{\frac{\theta}{2\pi}T}(\boldsymbol{X}_0) + \left((\Lambda^u)^{-\theta/(2\pi)} D\boldsymbol{\phi}_{\frac{\theta}{2\pi}T}(\boldsymbol{X}_0)\boldsymbol{V}^u\right)\xi^u + \left((\Lambda^s)^{-\theta/(2\pi)} D\boldsymbol{\phi}_{\frac{\theta}{2\pi}T}(\boldsymbol{X}_0)\boldsymbol{V}^s\right)\xi^s \quad (9)$$

is a parametrization of the linear approximation of the 3D stable–unstable manifold of the periodic orbit, since:

- If $\xi^u = \xi^s = 0$, it describes the periodic orbit as $0 \leq \theta \leq 2\pi$.
- For $\xi^s = 0$, $\xi^u \neq 0$, if $\theta = 0$ then $\boldsymbol{\psi}(\theta, \xi^u, \xi^s)$ is on the $\boldsymbol{V}^u$ eigenvector of the monodromy matrix. For $\theta \neq 0$, $\boldsymbol{\psi}(\theta, \xi^u, \xi^s)$ is on the vector transported from $\boldsymbol{V}^u$ through the differential of the flow, and

thus on the linear approximation of the unstable manifold of the p.o. The $(\Lambda^u)^{-\theta/(2\pi)}$ factor prevents stretching of the transported eigenvector, and keeps $\boldsymbol{\psi}(\theta, \xi^u, \xi^s)$ $2\pi$–periodic in $\theta$.

- For $\xi^u = 0$, $\xi^s \neq 0$, a symmetric argument applies.

A more formal way to see that Eqn. (9) parametrizes the linear approximation of the stable–unstable manifold of the periodic orbit is to check that, using the flow property ($\boldsymbol{\phi}_s(\boldsymbol{\phi}_t(\boldsymbol{X})) = \boldsymbol{\phi}_{t+s}(\boldsymbol{X})$) and the chain rule,

$$\boldsymbol{\phi}_t\big(\boldsymbol{\psi}(\theta, \xi^u, \xi^s)\big) = \boldsymbol{\psi}\big(\theta + \frac{2\pi}{T}t, (\Lambda^u)^{t/T}\xi^u, (\Lambda^s)^{t/T}\xi^s\big) + O\big((\xi^u)^2 + (\xi^s)^2\big), \tag{10}$$

which would be an invariance equation for $\boldsymbol{\psi}$ were not for the $O((\xi^u)^2 + (\xi^s)^2)$ term.

If we take the precaution of choosing both $\boldsymbol{V}^u$, and $\boldsymbol{V}^s$ pointing towards increasing longitudes of Vesta, due to the saddle dynamics of the linear approximation (from Eqn. (10), trajectories describe hyperbolae in ($\xi^u$, $\xi^s$) parameter space, that have $\boldsymbol{V}^u$, $\boldsymbol{V}^s$ as asymptotic directions in $\boldsymbol{X}$ space), and according to our previous definition of transit orbit, for fixed $\xi > 0$ small enough (for the linear approximation to be valid) and varying $\theta$, the initial conditions $\boldsymbol{\psi}(\theta, \xi, \xi)$ will produce transit orbits when integrated forward and backward in time.

### B. Sample 1:1 Resonance Crossing Ballistic Trajectories

For all the planar and vertical periodic orbits represented in Fig. 5, the values $\xi = 0.1, 1, 10\,\mathrm{km}$ are considered and the $50$ trajectories given by $\boldsymbol{\psi}(\theta, \xi, \xi)$ in Eqn. (9) for $\theta = j2\pi/50$ have been computed, integrating both forward and backward in time up to the vertical plane of the longitude of the fixed point plus $90$ degrees. Of all these trajectories, we have discarded those not being transit, that is, the ones not following the manifold branches of increasing longitudes of Vesta (as displayed in Fig. 8). Initial conditions for one such trajectory are provided in Table 6. For the given values of $\boldsymbol{X}_0, \theta, \boldsymbol{V}^u, \boldsymbol{V}^s$, $\boldsymbol{\psi}(\theta, \xi^u, \xi^s)$ provides a transit trajectory if $\xi^u = \xi^s = 1$, whereas it does not for $\xi^u = \xi^s = 10$ (the linear approximation is no longer valid). The corresponding trajectories are shown in Fig. 14.

After discarding the non–transit trajectories in the exploration just described, for each initial condition of each family and each value of $\xi$, we have plotted in Fig. 15 the difference between the maximum and minimum distance to the center of Vesta along the trajectories for varying $\theta$, as well as the minimum time of flight from the vertical plane of the longitude of the fixed point plus 90 degrees to itself.

**Table 6 Initial conditions for a sample planar Lyapunov transfer, to be used in Eqn. (9). The values $\boldsymbol{\phi}_{\frac{\theta}{2\pi}T}(\boldsymbol{X}_0)$, $D\boldsymbol{\phi}_{\frac{\theta}{2\pi}T}(\boldsymbol{X}_0))\boldsymbol{V}^u$, $D\boldsymbol{\phi}_{\frac{\theta}{2\pi}T}(\boldsymbol{X}_0))\boldsymbol{V}^s$, that require numerical integration with the first variationals, are provided for convenience.**

| Variables | Values |
|---|---|
| $\boldsymbol{X}_0$ | $($ 615.043543697725 , 169.512115103641 , 3.195465328012, |
| | $-0.055382713039651$ , 0.147098530261093 , $-0.001861017053890$ $)^\top$ |
| $T$ | 19617.67604385 |
| $\boldsymbol{V}^u$ | $($ $-0.483564088822$ , 0.875282662944 , $-0.006778552267$, |
| | $-0.000282281870382$ , $-0.000059016629411$ , $-0.000003748156386$ $)^\top$ |
| $\boldsymbol{V}^s$ | $($ $-0.197006162278$ , 0.980287095338 , $-0.015023323741$, |
| | $-0.000270703760181$ , $-0.000095925750484$ , $-0.000000523838148$ $)^\top$ |
| $\Lambda^u, \Lambda^s, \theta$ | 3.26466249952519 , 0.30631037669140 , $4\pi/5$ |
| $\boldsymbol{\phi}_{\frac{\theta}{2\pi}T}(\boldsymbol{X}_0)$ | $($ 414.503169532761 , 207.206280139795 , $-6.689909407586$, |
| | $-0.095972567216418$ , 0.194814529248627 , 0.001499981796764 $)^\top$ |
| $\boldsymbol{\phi}_{\frac{\theta}{2\pi}T}(\boldsymbol{X}_0)\boldsymbol{V}^u$ | $($ $-0.690401152398$ , 1.135695900648 , 0.006090577340, |
| | $-0.000502791172036$ , $-0.000217205538570$ , 0.000006766171830 $)^\top$ |
| $\boldsymbol{\phi}_{\frac{\theta}{2\pi}T}(\boldsymbol{X}_0)\boldsymbol{V}^s$ | $($ $-0.459465868763$ , 1.203211296360 , 0.016189252132, |
| | $-0.000464134492025$ , $-0.000265523893358$ , 0.000004245491819 $)^\top$ |

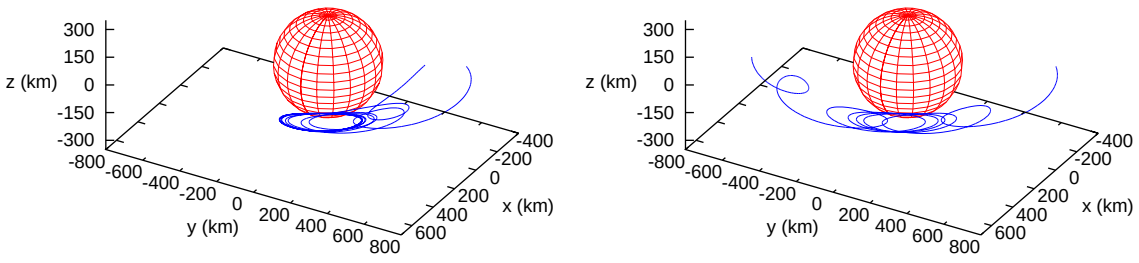


**Fig. 14 Trajectories with initial condition $\psi(\theta, \xi^u, \xi^s)$ according to the values of Table 6, for $\xi^u = \xi^s = 1$ (left) and $\xi^u = \xi^s = 10$ (right).**

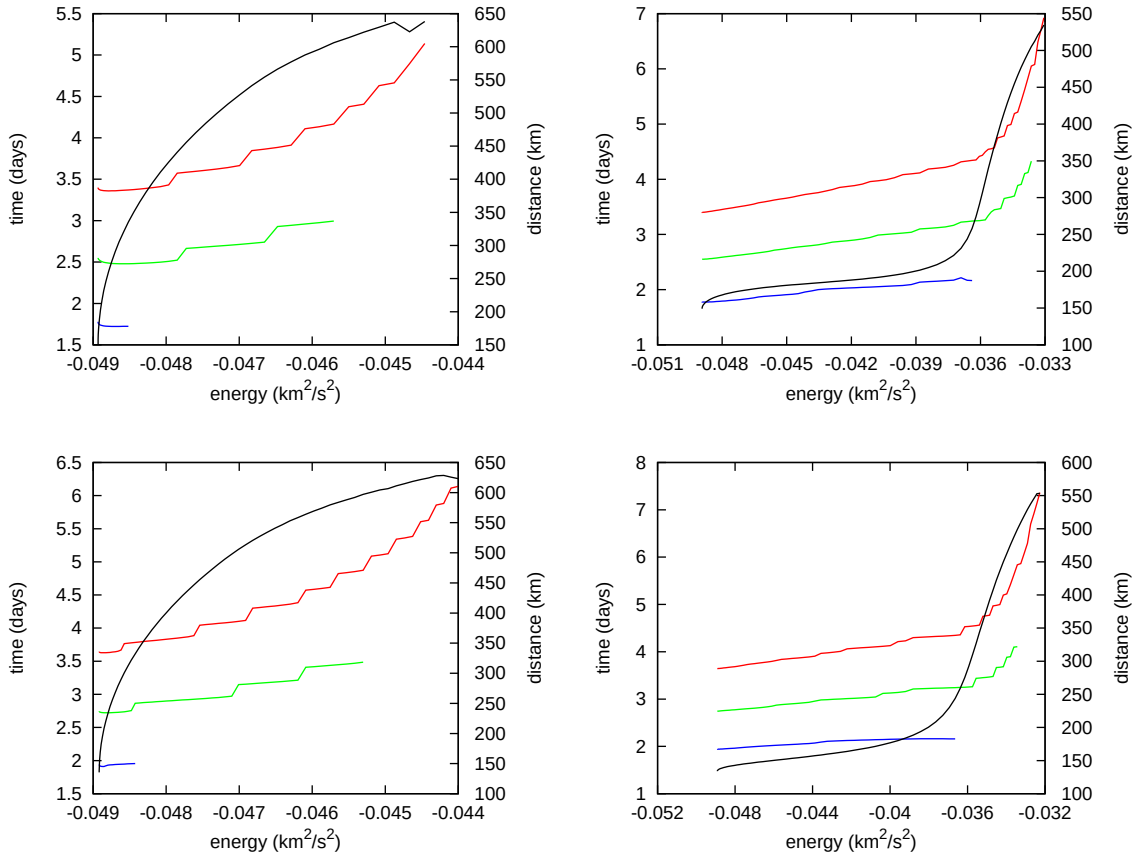


**Fig. 15 Some data on transit orbits approaching the planar (first column) and vertical (second column) families of Lyapunov orbits around $P_1$ (first row) and $P_3$ (second row). The red, green, and blue curves correspond to $\xi = 0.1$, 1 and $10\,\mathrm{km}$, respectively, and give the minimum time of flight (left $y$-axis) from the vertical plane of the longitude of the fixed point plus 90 degrees to itself. The black curves give the difference between the maximum and minimum distance to the center of Vesta, i.e., the potential ballistic transfer distance. At the scale of the plots, they are the same for the three values of $\xi$.**

In Fig. 15 it can be observed how, as the distance to the periodic orbit is increased, the time of flight decreases, because the trajectories perform fewer revolutions around the base periodic orbit as they approach and depart it. A side-effect to increasing $\xi$ is that the $\boldsymbol{\psi}(\theta, \xi, \xi)$ initial conditions stop providing transit trajectories sooner, which indicates that the linear approximation of the manifold is not accurate enough for these values of $\xi$. The difference between the maximum and minimum distances to the center of Vesta increase with the energy of the base periodic orbit, which is consistent with the constraints derived from the zero-velocity surface analysis. Figs. 16,17,18 display spatial views of a sample transfer of each family,

together with the time evolution of some orbital elements.

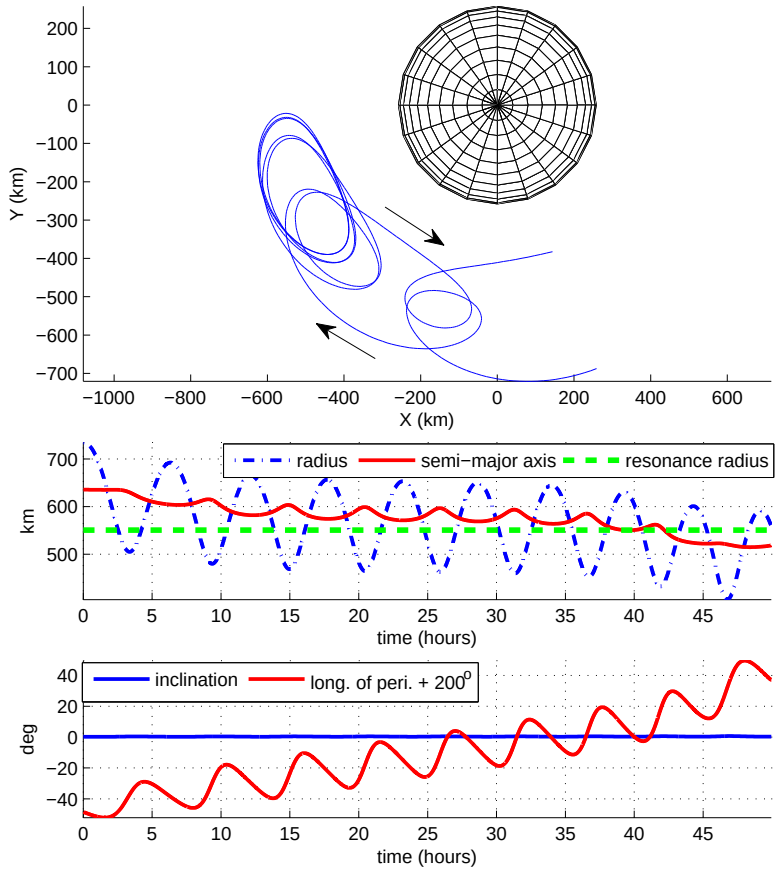


**Fig. 16 Sample resonance crossing transfer using the manifolds of a planar Lyapunov orbit. The top axes are plotted in the rotating body-fixed frame and the elements in the lower axes are computed in an inertial frame. In the rotating frame, the trajectory evolves clockwise initially (the period is sub-synchronous with the body rotation), then counter clockwise in the interior region.**

## VI. Conclusion

The stable and unstable manifolds of near-synchronous, unstable orbits in the body-fixed frame of an irregularly shaped body can be followed to achieve ballistic transfers across the 1:1 resonance. For low-thrust spacecraft, which must necessarily pass through a 1:1 resonant orbit *en route* to a super-synchronous orbit, the methodology presented herein identifies orbit targets that ensure passage across this region of chaotic

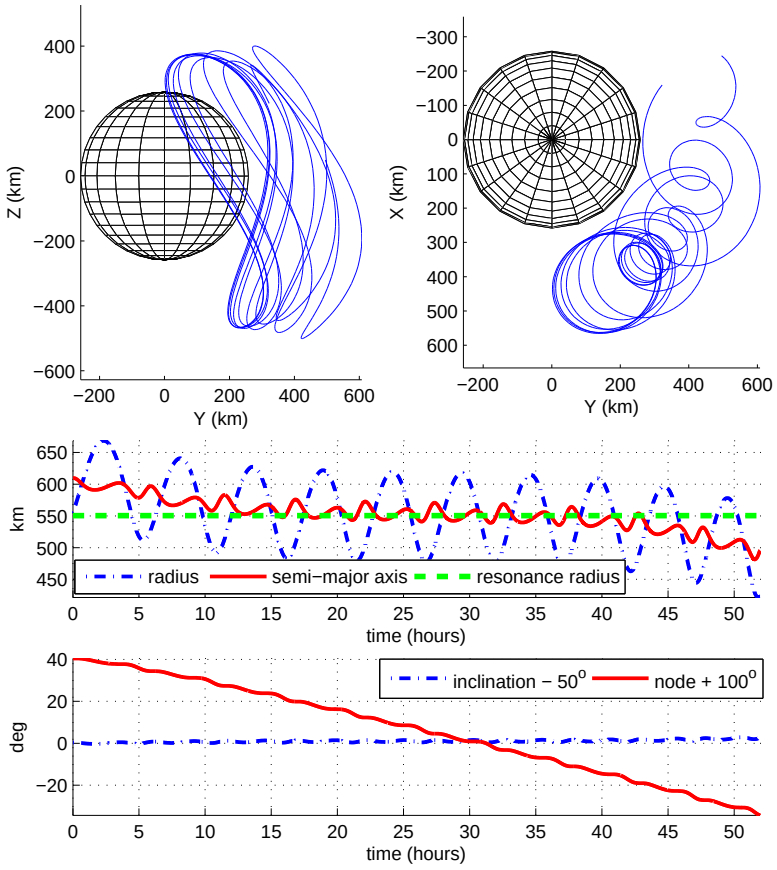


**Fig. 17 Sample resonance crossing transfer using the manifolds of a vertical Lyapunov orbit. The top axes are plotted in the rotating body-fixed frame and the elements in the lower axes are computed in an inertial frame. This middle inclination transfer results in significant variation in the node crossing longitude.**

dynamics. For the specific case of orbiting Vesta, these transfers have been shown to allow for a significant change in orbit altitude (on the order of $100$ km) without a change in orbit energy (i.e., without thrust) because of the relatively large deviation of Vesta's gravity from a pointmass. This transfer design strategy is well-suited for future low-thrust missions to asteroids and small planetary moons where the irregular gravity field similarly allows for large ballistic changes in an orbit near resonance, but requires careful targeting to ensure the desired change is achieved.

The sensitivity of this type of transfer to gravity field and other uncertainties remains to be studied. While hyperbolic equilibria and their associated dynamics are known theoretically to persist under small

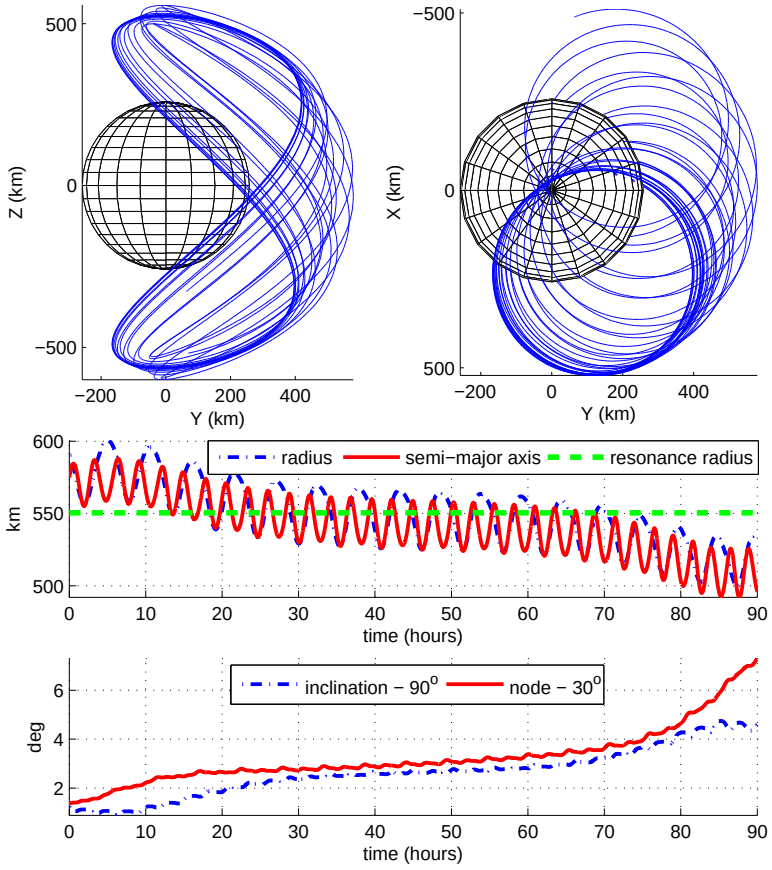


**Fig. 18 Sample resonance crossing transfer using the manifolds of a polar orbit. The top axes are plotted in the rotating body-fixed frame and the elements in the lower axes are computed in an inertial frame. Variations in the initial state can change the time for the transfer to complete.**

perturbations, the extent of their actual robustness is a question of significant practical importance.

### Appendix: Vesta Gravitational Field Model

As mentioned in the section "Dynamical Background", an $8\times8$ spherical harmonic gravity field has been used to model Vesta's gravitational potential. The coefficients for this model were generated by Alex Konopliv at the Jet Propulsion Laboratory at the California Institute of Technology using the Thomas shape model [14] with a constant density assumption[26]. This appendix provides a summary of the conventions and coefficients used.

**Table 7 Normalized spherical harmonic coefficients used to define the gravitational potential of Vesta.**

| | | | | | | | |
|---|---|---|---|---|---|---|---|
| $\overline{C}_{0,0}$ | 1.00000000000e+00 | $\overline{S}_{0,0}$ | 0.00000000000e+00 | $\overline{C}_{6,2}$ | –1.56976008416e–04 | $\overline{S}_{6,2}$ | –3.26673192977e–05 |
| $\overline{C}_{1,0}$ | 0.00000000000e+00 | $\overline{S}_{1,0}$ | 0.00000000000e+00 | $\overline{C}_{6,3}$ | –3.99739451316e–05 | $\overline{S}_{6,3}$ | 4.56863652413e–04 |
| $\overline{C}_{1,1}$ | 0.00000000000e+00 | $\overline{S}_{1,1}$ | 0.00000000000e+00 | $\overline{C}_{6,4}$ | 3.77321609708e–04 | $\overline{S}_{6,4}$ | 1.22025762333e–04 |
| $\overline{C}_{2,0}$ | –4.07805507010e–02 | $\overline{S}_{2,0}$ | 0.00000000000e+00 | $\overline{C}_{6,5}$ | –2.02585801195e–04 | $\overline{S}_{6,5}$ | –1.73238620246e–04 |
| $\overline{C}_{2,1}$ | –3.25010390544e–04 | $\overline{S}_{2,1}$ | 1.49720853708e–03 | $\overline{C}_{6,6}$ | 6.77387913531e–05 | $\overline{S}_{6,6}$ | 7.48949709186e–05 |
| $\overline{C}_{2,2}$ | 4.46821319973e–03 | $\overline{S}_{2,2}$ | 4.61382771891e–03 | $\overline{C}_{7,0}$ | 5.70293656227e–04 | $\overline{S}_{7,0}$ | 0.00000000000e+00 |
| $\overline{C}_{3,0}$ | 3.64651747993e–03 | $\overline{S}_{3,0}$ | 0.00000000000e+00 | $\overline{C}_{7,1}$ | 3.98235640002e–04 | $\overline{S}_{7,1}$ | 7.24405013000e–04 |
| $\overline{C}_{3,1}$ | –1.12409582062e–03 | $\overline{S}_{3,1}$ | –3.89500727795e–04 | $\overline{C}_{7,2}$ | 3.56046364969e–04 | $\overline{S}_{7,2}$ | 3.87838248289e–04 |
| $\overline{C}_{3,2}$ | –1.16408456814e–03 | $\overline{S}_{3,2}$ | –7.62581870322e–04 | $\overline{C}_{7,3}$ | –3.33397472073e–04 | $\overline{S}_{7,3}$ | 3.20233884344e–05 |
| $\overline{C}_{3,3}$ | –6.72307486207e–04 | $\overline{S}_{3,3}$ | 5.48451210418e–04 | $\overline{C}_{7,4}$ | –8.02300909991e–05 | $\overline{S}_{7,4}$ | 4.54688133019e–05 |
| $\overline{C}_{4,0}$ | 5.65283691159e–03 | $\overline{S}_{4,0}$ | 0.00000000000e+00 | $\overline{C}_{7,5}$ | –8.70846159655e–05 | $\overline{S}_{7,5}$ | 2.17960394084e–04 |
| $\overline{C}_{4,1}$ | 1.27115944748e–03 | $\overline{S}_{4,1}$ | –1.61833763492e–04 | $\overline{C}_{7,6}$ | 2.10488488560e–04 | $\overline{S}_{7,6}$ | 9.74422338716e–05 |
| $\overline{C}_{4,2}$ | –5.69178351863e–04 | $\overline{S}_{4,2}$ | 8.92221404608e–05 | $\overline{C}_{7,7}$ | 1.62511871062e–04 | $\overline{S}_{7,7}$ | 1.34280339470e–04 |
| $\overline{C}_{4,3}$ | –2.51263799636e–04 | $\overline{S}_{4,3}$ | –8.05756564163e–04 | $\overline{C}_{8,0}$ | –9.93386709112e–05 | $\overline{S}_{8,0}$ | 0.00000000000e+00 |
| $\overline{C}_{4,4}$ | –4.74265577836e–04 | $\overline{S}_{4,4}$ | 2.74536736864e–04 | $\overline{C}_{8,1}$ | 3.64907867445e–06 | $\overline{S}_{8,1}$ | 1.42310868220e–04 |
| $\overline{C}_{5,0}$ | –2.09370174402e–03 | $\overline{S}_{5,0}$ | 0.00000000000e+00 | $\overline{C}_{8,2}$ | –1.06843394510e–04 | $\overline{S}_{8,2}$ | –1.89336591209e–04 |
| $\overline{C}_{5,1}$ | 2.44608680997e–05 | $\overline{S}_{5,1}$ | 1.27062948281e–04 | $\overline{C}_{8,3}$ | 1.26356875251e–04 | $\overline{S}_{8,3}$ | 1.02541745679e–04 |
| $\overline{C}_{5,2}$ | 3.90449578804e–04 | $\overline{S}_{5,2}$ | –2.60096374968e–04 | $\overline{C}_{8,4}$ | –1.65491066823e–04 | $\overline{S}_{8,4}$ | 5.96662177612e–05 |
| $\overline{C}_{5,3}$ | 4.44827891684e–04 | $\overline{S}_{5,3}$ | –2.66156245454e–04 | $\overline{C}_{8,5}$ | 1.27714821210e–04 | $\overline{S}_{8,5}$ | 5.13750623888e–05 |
| $\overline{C}_{5,4}$ | 1.69785526541e–04 | $\overline{S}_{5,4}$ | –7.68917712397e–04 | $\overline{C}_{8,6}$ | –2.12747942358e–04 | $\overline{S}_{8,6}$ | 7.84398845706e–05 |
| $\overline{C}_{5,5}$ | –3.02983473394e–05 | $\overline{S}_{5,5}$ | –8.97643036386e–05 | $\overline{C}_{8,7}$ | 1.29147008848e–04 | $\overline{S}_{8,7}$ | –7.63161885204e–05 |
| $\overline{C}_{6,0}$ | –5.07091621859e–04 | $\overline{S}_{6,0}$ | 0.00000000000e+00 | $\overline{C}_{8,8}$ | 3.61889312604e–05 | $\overline{S}_{8,8}$ | 7.24673054196e–05 |
| $\overline{C}_{6,1}$ | –6.72234557467e–04 | $\overline{S}_{6,1}$ | –6.49425559362e–04 | | | | |

In all the results reported in this paper, the gravitational potential of Vesta at a point $\tilde{\mathbf{r}} = (x, y, z)$ has been expressed in the body fixed frame defined in the "Dynamic background" section. Its expression in that frame is given by:

$$U(\tilde{\mathbf{r}}) = \frac{\mu}{r} \sum_{n=0}^{8} \sum_{m=0}^{n} \Big(\frac{R_V}{r}\Big)^n \overline{P}_{n,m}(\sin\phi)\big(\overline{C}_{n,m}\cos(m\lambda) + \overline{S}_{n,m}\sin(m\lambda)\big), \tag{11}$$

where $\mu$ denotes the gravitational parameter of Vesta ($17.8\ \mathrm{km}^3/\mathrm{s}^2$) and $R_V$ corresponds to the radius of the reference sphere of the expansion in spherical harmonics ($258\ \mathrm{km}$). The spherical coordinates used $(r, \phi, \lambda)$

are defined as $x = r\cos\phi\cos\lambda$, $y = r\cos\phi\sin\lambda$, $z = r\sin\phi$, and the various $\overline{C}_{n,m}$ and $\overline{S}_{n,m}$ used are given in Table 7.

Note that the normalized spherical harmonics and coefficients are used, following the convention in reference [21] p. 58. In particular, the normalized Legendre associated functions are defined by:

$$\overline{P}_{n,m}(u) = \sqrt{\frac{(2-\delta_{0,m})(2n+1)(n-m)!}{(n+m)!}} P_{n,m}(u) \tag{12}$$

with $P_{n,m}(u) = (1-u^2)^{m/2}\frac{d^m}{du^m}P_n(u)$ and $P_n(u) = \frac{1}{2^n n!}\frac{d^n}{du^n}(u^2-1)^n$.


**Acknowledgments**

The authors would like to thank Greg Whiffen of the Dawn navigation team at Jet Propulsion Laboratory for sharing his opinions, data, and time in support of this study. The authors also thank Alex Konopliv of the Jet Propulsion Laboratory for providing the gravity model of Vesta described in the Appendix based on pre-Dawn encounter data. J.M. Mondelo is supported by the Spanish MCyT/FEDER grant MTM2008–01486, the Spanish MCyT/FEDER grant MTM2006-05849/Consolider, and the Catalan grant 2009SGR410. Part of this work as been performed at the Jet Propulsion Laboratory, California Institute of Technology, which is under contract with the National Administration for Space and Aeronautics.


**References**


[1] Rayman, M. D., Fraschetti, T. C., Raymond, C. A., and Russell, C. T., "Dawn: A mission in development for exploration of main belt asteroids Vesta and Ceres," *Acta Astronautica*, Vol. 58, 2006, pp. 605–616.

[2] Raymond, C. A. and Russell, C. T., "Exploring Asteroid 4 Vesta with the Dawn Mission," abstract presented at the 41st Lunar and Planetary Science Conference, Woodlands, TX, March 1-5.

[3] A.Morbidelli, *Modern Celestial Mechanics; Aspects of Solar System Dynamics*, Taylor & Francis; Available online on the author webpage, 2006.

[4] Warner, B., Harris, A., and Pravec, P., "The Asteroid Lightcurve Database," *Icarus*, Vol. 202, pp. 134–146, Rev. 2011-Dec-17. Updates available at `http://www.minorplanet.info/lightcurvedatabase.html`.

[5] Tricarico, P. and Sykes, M., "The dynamical environment of Dawn at Vesta," *Planetary and Space Science*, Vol. 58, 2010, pp. 1516–1525.

[6] Delsate, N., "Analytical and numerical study of the ground-track resonances of Dawn orbiting Vesta," *Planetary and Space Science*, Vol. 59, 2011, pp. 1372–1383.

[7] Conley, C. C., "Low energy transit orbits in the restricted three-body problem," *SIAM J. Appl. Math.*, Vol. 16, 1968, pp. 732–746.

[8] McGehee, R. P., *Some homoclinic orbits for the restricted three-body problem*, Ph.D. thesis, University of Wisconsin, 1969.

[9] Koon, W. S., Lo, M. W., Marsden, J. E., and Ross, S. D., "Heteroclinic Connections between Periodic Orbits and Resonance Transitions in Celestial Mechanics," *Chaos*, Vol. 10, No. 2, 2000, pp. 427–469.

[10] Russell, R. P. and Lam, T., "Designing Ephemeris Capture Trajectories at Europa Using Unstable Periodic Orbits," *Journal of Guidance, Control, and Dynamics*, Vol. 30, No. 2, 2007, pp. 482–491.

[11] Kaula, W. M., *Theory of Satellite Geodesy*, Blaisdell; reprint by Dover, Waltham, Massachusetts, 1966.

[12] Scheeres, D. J., "Dynamics About Uniformly Rotating Tri-Axial Ellipsoids. Applications to Asteroids," *Icarus*, Vol. 110, No. 2, 1994, pp. 225–238.

[13] Thomas, P. C., Binzel, R. P., Gaffey, M. J., Storrs, A. D., Wells, E., and Zellner, B. H., "Impact Excavation on Asteroid 4 Vesta: Hubble Space Telescope Results," *Science*, Vol. 277, 1997, pp. 1492–1495.

[14] Thomas, P. C., Binzel, R. P., Gaffey, M. J., Zellner, B. H., Storrs, A. D., and Wells, E., "Vesta: Spin Pole, Size and Shape from HST Images," *Icarus*, Vol. 128, 1997, pp. 88–94.

[15] Busch, M., Giorgini, J., Ostro, S., Benner, L., Jurgens, R., Rose, R., Hicks, M., Pravec, P., Kusnirak, P., Ireland, M., Scheeres, D., S.B. Broschart, C., Magri, Nolan, M., Hine, A., and Margot, J.-L., "Physical Modeling of near-Earth Asteroid (29075) 1950 DA," *Icarus*, Vol. 190, No. 2, 2007, pp. 608–621.

[16] Meyer, K. R., Hall, G. R., and Offin, D., *Introduction to Hamiltonian Dynamical Systems and the $N$–Body Problem*, Springer–Verlag, 2nd ed., 2009.

[17] Hénon, M., "Exploration Numérique du Problème Restreint. II: Masses égales, stabilité des orbites periódiques," *Annales d'Astrophysique*, Vol. 28, No. 6, 1965, pp. 992.

[18] Gómez, G. and Mondelo, J. M., "The dynamics around the collinear equilibrium points of the RTBP," *Phys. D*, Vol. 157, No. 4, 2001, pp. 283–321.

[19] Cunningham, L. E., "On the computation of the spherical harmonic terms needed during the numerical integration of the orbital motion of an artificial satellite," *Celestial Mech.*, Vol. 2, 1970/1971, pp. 207–216.

[20] Gómez, G., Koon, W. S., Lo, M. W., Marsden, J. E., Masdemont, J., and Ross, S. D., "Connecting orbits and invariant manifolds in the spatial restricted three-body problem," *Nonlinearity*, Vol. 17, No. 5, 2004, pp. 1571–1606.

[21] Montenbruck, O. and Gill, E., *Satellite Orbits. Models, Methods and Applications*, Springer-Verlag, 2000.

[22] A first idea of the instability of the resonant zone can be obtained from the $\lambda^j$ values of Table 3.

[23] An interesting subject not addressed in this paper is to study this interaction. Random numerical experiments have

revealed the existence of trajectories following heteroclinic connections of $P_1$ and $P_3$..

[24] Two stable orbit families were also found near $P_2$ and $P_4$, but these are not useful for the type of transfers being discussed in this paper.

[25] The non-physical continuation of the polar family around $P_1$ after impact with the reference sphere of Vesta reveals a complex network of families of periodic orbits, without showing a simple connection with the vertical Lyapunov familiy.

[26] This model is based entirely on data available before the Dawn mission encounter with Vesta and in no way reflects the observational findings of the Dawn mission.